UNIVERSITEIT VAN PRETORIA
UNIVERSITY OF PRETORIA
YUNIBESITHI YA PRETORIA

School of Engineering
University of Pretoria

MODELLING OF NON-LINEAR AEROELASTIC SYSTEMS USING A STRONGLY COUPLED FLUID-STRUCTURE-INTERACTION METHODOLOGY

Andrew G. B. Mowat

Supervisors: A.G. Malan and J.P. Meyer

Thesis submitted to the University of Pretoria in candidature
for the degree of Masters in Engineering

September 2011

This work is dedicated to my parents, Paul and Mynie.

Abstract

The purpose of this study was to develop a robust fluid-structure-interaction (FSI) technology that can accurately model non-linear flutter responses for sub- and transonic fluid flow. The Euler equation set governs the fluid domain, which was spatially discretised by a vertex-centred edge-based finite volume method. A dual-timestepping method was employed for the purpose of temporal discretisation. Three upwind schemes were compared in terms of accuracy, efficiency and robustness, viz. Roe, HLLC (Harten-Lax-Van Leer with contact) and AUSM^{+}-up (Advection Up-stream Splitting Method). For this purpose, a second order unstructured MUSCL (Monotonic Upstream-centred Scheme for Conservation Laws) scheme, with van Albada limiter, was employed. The non-linear solid domain was resolved by a quadratic modal reduced order model (ROM), which was compared to a semi-analytical and linear modal ROM. The ROM equations were solved by a fourth order Runge-Kutta method. The fluid and solid were strongly coupled in a partitioned fashion with the information being passed at solver sub-iteration level. The developed FSI technology was verified and validated by applying it to test cases found in literature. It was demonstrated that accurate results may be obtained, with the HLLC upwind scheme offering the best balance between accuracy and robustness. Further, the quadratic ROM offered significantly improved accuracy when compared to the linear method.

Acknowledgements

I would like to acknowledge and thank my supervisor, Dr Arnaud Malan for his continued guidance and support, he has been an inspiration to me and I am grateful for his input in this work. I also would like to thank my co-supervisor Prof Josua Meyer for his support and financial backing. To the other five members of the 'Magnificent Seven', Oliver, Johan, Ridwaan, Nathan and Johann, I am grateful for your advice and the many cups of great coffee. Lastly, to my friends, family and beautiful wife, thank you for all your love, prayers and words of encouragement.

The funding obtained from the NRF, TESP, University of Stellenbosch, University of Pretoria, SANERI/SANEDI, CSIR, EEDSM Hub and NAC is acknowledged and duly appreciated.

Contents

Nomenclature

Greek Symbols

α	Angle-of-attack (°)
α_0	Mean angle-of-attack (°)
α_{max}	Maximum angle-of-attack (°)
$\hat{\alpha}$	Wave strength
$\tilde{\alpha}$	Parameter used in AUSM$^+$-up scheme
β	Parameter used in AUSM$^+$-up scheme
γ	Ratio of specific heats. Taken as 1.4 for air
ε	Difference of calculated solutions
κ	Runge-Kutta weighting coefficient
$\hat{\lambda}$	Eigenvalues of the Jacobian Matrix
μ	Airfoil mass ratio, $\mu = \frac{m}{\pi \rho b^2}$
ρ	Density
$\hat{\rho}$	Roe average density
σ	Parameter used in AUSM$^+$-up scheme
τ	Pseudo time
ϕ	Upwind variable used in the MUSCL scheme
Φ	Vector of force vectors
ψ	Limiter function
$\vec{\psi}$	Convected variables
Ψ	Constant matrix of structural parameters

Υ_{mn}	Refers to the edge connecting nodes m and n
ω	Relaxation factor
ω_α	Uncoupled pitch natural frequency
ω_h	Uncoupled plunge natural frequency

Mathematical Operators

$\Delta\bullet$	Increment in $\bullet$
δ_{ij}	Kronecker delta function: unity if $i = j$ and zero if $i \neq j$
∇	Gradient operator
$\ddot{\ }$	Second-derivatives with respect to time

Roman Symbols

a	Position of the elastic centre, measured from the mid-chord along the chord when the airfoil is at rest
b	Semi-chord length
c	Acoustic velocity
c	Chord length
$\hat{c}$	Roe average acoustic velocity
$\tilde{c}$	Critical acoustic velocity
$\mathbf{C}$	Edge coefficient
CFL	Courant-Friedrichs-Lewy number
C_{L}	Sectional lift coefficient
C_{M}	Sectional moment coefficient
C_p	Specific heat at constant pressure (J/kgK)
C_v	Specific heat at constant volume (J/kgK)
D	Distances to identified boundary points
$\mathcal{D}$	Number of dimensions represented by the mesh
E	Total specific energy
f	Estimated solution

f_a	Scaling factor
f_{extrap}	Richardson Extrapolated approximate zero grid spacing solution
$\mathbf{f}$	Aerodynamic force at node
$\mathbf{F}$	Flux vector
$\overline{\mathbf{F}}$	Upwinded flux vector
$\mathcal{F}_s$	Safety factor
$\hat{\mathbf{g}}$	Normalised quadratic mode shape
G	Riemann invariant
GCI	Grid Convergence Index
h	Vertical displacement (positive down)
$\mathtt{h}$	Structural timestep size
H	Total specific enthalpy
$\hat{H}$	Roe average specific enthalpy
I_α	Sectional moment of inertia of the airfoil
$\mathbf{I}$	Identity matrix
k_c	Reduced frequency
K_α	Pitching spring coefficient
K_h	Plunging spring coefficient
K_p	Pressure diffusion coefficient
K_u	Velocity diffusion coefficient
$\mathbf{K}$	Stiffness matrix
$\hat{\mathbf{K}}$	Eigenvectors of the Jacobian Matrix
L	Characteristic length
L	Sectional lift per unit span
m	Mass of the airfoil per unit span
$\dot{m}$	Mass flux
M	Mach number

M_α	Sectional moment about the elastic centre (positive nose up)
M_o	Reference Mach number
M_p	Pressure diffusion term
$\mathcal{M}$	Split Mach number
$\overline{M}$	Mean local Mach number
$\mathbf{M}$	Mass matrix
n_j	Unit normal in the j-direction
$\mathbf{n}$	Unit normal vector
N	Mesh size
p	Pressure
$\mathtt{p}$	Order accuracy of the solution
$\mathbf{p}$	Pressure flux
$\mathcal{P}$	Split pressure function
$\mathbf{q}$	Displacement vector
$\mathbf{Q}$	Generalised force vector
$\hat{Q}$	Generalised force vector
r	Ratio of consecutive solution variables
r_α	Structural parameters, $r_\alpha^2 = \frac{I_\alpha}{mb^2}$
r	Distance from where the force is applied to the elastic centre
$\mathtt{r}$	Grid refinement ratio
$\mathtt{r}_b$	Ratio of distances to the identified boundary points
$\mathbf{r}$	Dependent variable solved for in structure response
R	Gas constant (J/kgK). Taken as $287J/kgK$ for air
$\hat{R}$	Ratio of left and right state densities
$\mathbf{R}$	Right-hand side of algebraic equation
S	Wave speed
$\mathcal{S}$	Surface

$\mathbf{S}$	Source term
S_α	Static imbalance
S_M	Middle wave speed used in HLLC scheme
t	Time
T	Temperature
u	Velocity
$\mathbf{u}$	Velocity vector
u_n	Velocity magnitude normal to the boundary
$\hat{u}$	Roe average velocity
$\hat{\mathbf{u}}$	Normalised linear mode shape
$\mathbf{U}$	Dependant conservative variables vector
U_∞	Free stream velocity
v	Moving reference frame velocity
$\mathbf{v}$	Moving reference frame velocity vector
V	Volume
V_F	Flutter speed
$\mathcal{V}$	Computational volume
w	Relative velocity to the moving reference frame
x_j	Position coordinates in the j-direction
$\mathbf{x}$	Vector of position coordinates
$\mathbf{x}_0$	Position of the elastic centre
x_α	Structural parameters, $x_\alpha = \frac{S_\alpha}{mb}$
x_r	Position of node when the airfoil is at rest
$\delta\mathbf{x}_1$	Displacements of the closest internal boundary points
$\delta\mathbf{x}_2$	Displacements of the closest external boundary points
Δx	Average edge length over the surface of the airfoil

Superscripts

i	Superscript index
j	Superscript index
k	Superscript index
L	Left state index
mn	Quantities denote edge-face values
n	Timestep number
R	Right state index
$*$	Dimensional quantity
$\star$	Variables related to the middle wave speed in HLLC scheme
τ	Pseudo-timestep number

Subscripts

b	Boundary entity
e	Extrapolated quantity
f	Fluid parameter
∞	Subscript denotes free stream value
j	Subscript index
k	Subscript index
L	Left state index
l	Subscript index
m	Node index
mn	Quantities denote edge-face values
n	Node index
R	Right state index
s	Solid parameter

All symbols in this nomenclature are non-dimensional, unless stated otherwise, and a repeated index indicates the use of Einstein summation convention.

List of Figures

List of Tables

Chapter 1

Introduction

1.1 Background and Project Motivation

Aeroelastics is the study of the dynamic interaction between a flexible structure and the aerodynamic forces resulting from surrounding fluid flow [2]. The field of aeroelastics has many facets which are aptly summed up in Collar's aeroelastic triangle [1], shown in Figure 1.1. In the figure, *Inertial Forces* refers to the field of Dynamics, as *Elastic Forces* to Solid Mechanics and *Aerodynamic Forces* to Fluid Dynamics. The combination of these separate fields is represented on the edges of the triangle. Aeroelastics is the combination of all three fields, as shown in the centre.

There are many industries that have an interest in Aeroelastics, but one of the largest is the Aerospace industry. This is due to wings of aircraft being

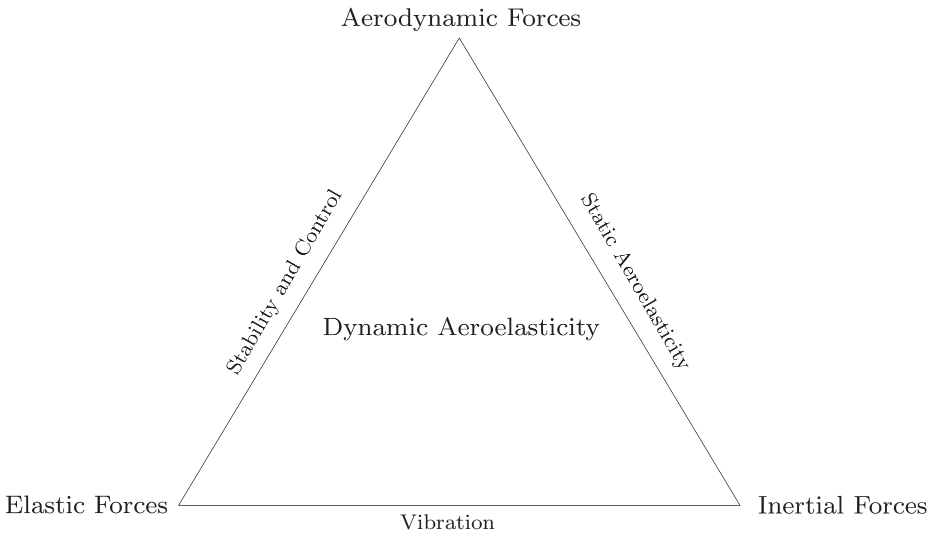

Figure 1.1: Collar's [1] Aeroelastic Triangle

long and flexible structures that operate under aerodynamic loads to lift the aircraft. This results in a multitude of complex fluid-structure interaction dynamics which should be given careful consideration in the interest of safety and desired operation [3]. One such a phenomenon is the unstable amplifying vibration of a wing due to the aerodynamic loads, which is known as flutter. Flutter is arguably one of the aeroelastic phenomena of central interest to the aerospace industry as it may result in catastrophic failure of the structure [1, 4–6]. Buffeting is another example of an unwanted aeroelastic phenomenon, which is caused by unsteady loading on a structure due to sustained rapid velocity fluctuations. These vibrations greatly decrease the service life of an aircraft [7]. As a result, computational modelling technologies today play a pivotal role in its prediction and prevention.

The present day aerospace industry has a well-established understanding of linear flutter phenomena at sub-sonic flow speeds, with numerous established techniques being available [8]. There is still, though, much progress required to effect efficient fluid-structure-interaction (FSI) modelling in the transonic flow regime, particularly where a combination of sonic shocks in the fluid domain and non-linear structural responses are present. These, for example, violate the predictions of standard linear velocity potential methods [9,10]. This has led to the growth of Computational Aeroelastics, which looks to find more detailed and effective methods with which to model non-linear aeroelastics [11]. This includes the development of full aeroelastic modelling techniques on realistic geometries [10, 12–23].

Non-linear aeroelastic FSI algorithms may be broadly sub-divided in terms of the coupling effected between the fluid and the solid domains, viz. strong and weak coupling. Weakly coupled fluid-solid modelling does not enforce rigorous simultaneous satisfaction of fluid and solid governing equations at each timestep. An example is staggered time-stepping, which is widely used and found to be computationally efficient [16, 24]. However, when applied to strongly coupled FSI systems, the aforementioned may be prone to inaccurate or divergent solutions [25–28]. Strongly coupled modelling techniques, on the other hand, enforce simultaneous solution of both fluid and structure, and may be classified into two groups: partitioned and simultaneous solution monolithic methods. The latter [25, 26] effects solutions via a single matrix. Partitioned methods discretise the fluid and structure domains separately, where coupling may be effected in an efficient manner via non-linear iterations [28–31].

For the purpose of aerodynamics, it is typical to describe the fluid as a continuum, from which the Navier-Stokes partial differential equation set results. This constitutes the defacto standard to quantitatively describe the mechanics of a fluid under flow conditions which range from sub- to transonic. As flutter under typical aerodynamic operation conditions is generally driven by pressure distribution (lift and moment), the Euler equation subset is viewed as suitable to describe aerodynamic flows which do not contain large-scale flow separation [3, 32–36]. In this work an Arbitrary Lagrangian-Eulerian (ALE) formulation is employed to accommodate an arbitrary moving reference frame, i.e. the solid in the fluid domain. It is not currently tractable to construct an analytical solution to the Euler equation set in the general case, thus we discretise the fluid domain and solve it numerically.

The numerical methods most commonly used to obtain solutions to the Euler equation set belong to the methods of weighted residuals, viz. finite difference, finite element and finite volume methods. The finite difference method is the earliest method to be utilised and remains problematic to generate on complex geometries. The finite element (FE) method was originally only used for structural analysis but has been adapted, since the 90's, to model fluids as well. In certain cases, the FE method has been found to be numerically equivalent to the finite volume approach but is more complex and can be computationally more expensive [37]. Thus the finite volume method is the popular choice in the context of spatially second-order accurate Computational Fluid Dynamics (CFD), of which two variants exist, viz. the cell-centred and the vertex-centred scheme. Within each of these methods various schemes exist by which the convective flux can be discretised. These schemes, aim to avoid non-physical instabilities in the fluid domain or odd-even decoupling. For the purpose of this study we will focus on vertex-centred second-order accurate method, which is preferable as it is computationally more efficient than the cell-centred version on unstructured meshes [38].

The Euler equation set is convection-dominated, for which two main groups of methods are used to spatially discretise the convective flux. The first is known as the central schemes, which is based on the central difference formula and uses artificial dissipation [39] to prevent odd-even decoupling. The second group is referred to as upwind schemes which fall into one of four categories, viz. Flux-Vector Splitting schemes, Flux-Difference Splitting schemes, Total Variation Diminishing (TVD) schemes and Fluctuation-Splitting schemes. Flux-vector splitting schemes decompose the convective flux vector into two parts according to criteria related to the characteristic variables. Examples are the Advection Upstream Splitting Method (AUSM) [40–42] and Convection Upwind Split Pressure (CUSP) schemes [43]. These are popular due to the improved resolution of the shear layer with moderate computational effort, while being extendible to real gas flows. The Flux-differencing method aims to solve the one-dimensional Euler equation for discontinuous states locally. Godunov [44] introduced the idea and approximate Riemann solvers resulted, such as Roe [45], Osher [46] and HLL (Harten-Lax-Van Leer) [47] which led to the HLLC scheme (C stands for contact) [48]. Roe's [45] upwind scheme has been widely used for its robust ability to represent shocks and its resolution of the boundary layer. TVD schemes have limited use as they cannot be readily extended to second-order spacial accuracy, though methods have been developed to overcome the problem [49]. These schemes can be combined with matrix dissipation schemes. This creates a scheme that has favourable upwind algorithmic behaviour in the region of the flow discontinuity, while using the computationally more efficient central-difference scheme over the remainder of the flow domain [50]. The use of Fluctuation-Splitting schemes has various benefits due to its ability to account for flow features that are not aligned with the mesh. It is, however, generally only implemented for research applications because of its high computational cost, complexity and poor convergence. The importance of transonic flow, to this study, necessitates the use of a robust and accurate flux discretisation method with shock-capturing ability.

The solid domain can be resolved using one of two general methods, viz. detailed finite element modelling (FEM) or reduced order modelling (ROM). In this study, we consider aircraft wings, which in reality are complex structures composed of a multitude of plates and fasteners. Resolving the stresses in each component for the purpose of aeroelastic analysis would be superfluous. The use of a ROM from which airfoil surface deflections may be calculated is thus more pragmatic. A ROM constitutes a mathematical representation which describes the dominant physics of interest at considerably reduced computational cost when compared to the detailed model [51]. Modal analysis has been used with success in aerospace to construct ROMs of the structure [52]. Such ROMs are typically able to describe linear motion, i.e. displacement along a straight line, which has shown to be accurate in certain cases [53, 54]. However, where torsional modes are significant, as in the flutter response of certain airfoil geometries, the linear ROMs become inaccurate and a quadratic ROM is required [54]. This is due to the ability of the quadratic ROM to prescribe the motion of a point on the structure with a curved path [54–56].

1.2 Overview and Purpose of Study

The FSI algorithm developed in this work is a strongly coupled partitioned method where information is passed between the fluid and solid domains at solver sub-iteration level. This results in a fully-converged solution at each timestep where both dynamic and kinematic continuity are satisfied at the fluid-solid interface. To account for the transonic shocks, the fluid is described via the compressible Euler equations written in an ALE reference frame [32–36]. A vertex-centred edge-based finite volume method for spacial discretisation was used due to it being both computationally efficient, as well as being well suited to parallel computing. To effect shock capturing and suppress non-physical oscillations, three upwind schemes were investigated, viz. Roe scheme [45], HLLC scheme [48] and AUSM^{+}-up scheme [42]. These schemes were selected on robustness and accuracy considerations, and ALE versions were implemented. The MUSCL scheme [57] with the van Albada limiter [58] was used for the purpose of upwinding with shock capturing. Fourth-order Runge-Kutta and dual-time-stepping methods were employed respectively for solution and temporal discretisation, in conjunction with parallel computing.

The structure is represented via a quadratic modal ROM [55, 56, 59]. This is of particular interest due to its ability to describe non-linear motion from linear modal data. It is also readily extendible to three-dimensional systems. The fluid and solid domains, where information is passed between the detailed CFD and structural ROM at each sub-iteration, are strongly coupled numerically.

The developed FSI technology was implemented into the multi-physics code Elemental, followed by a verification and validation exercise. The accuracy and robustness of the three upwind schemes was assessed via application to both the classic shock tube test case [60], as well as the forced oscillation of a NACA0012 airfoil under transonic flow. The evaluation included a grid convergence study. Next, the two-dimensional flutter-response of a pitch-plunge airfoil was considered at sub- to transonic flow speeds over a NACA64A010 airfoil section. The improvement in accuracy of the quadratic modal ROM over the traditional linear modal ROM was assessed by comparison to a semi-analytical method.

1.3 Thesis Layout

The thesis is divided into five chapters, a short summary of each chapter is given below.

- **Chapter 1**. **Introduction**. In this chapter the background of the work is discussed along with an overview of the work completed in this thesis. The publications resulting from this work are given at the end of the chapter.

- **Chapter 2**. **Governing Equations**. The equations employed to describe the fluid and solid domain are detailed in this chapter.

- **Chapter 3**. **Numerical Solution Procedure**. The chosen spacial and temporal discretisation algorithms for the fluid domain, as well as the semi-analytical, linear and quadratic ROMs of the solid domain are detailed in this chapter. The fluid-solid interaction modelling methodology is described along with the solution procedure. Lastly, the parallelisation of the developed FSI algorithm is detailed.

- **Chapter 4**. **Results and Evaluation**. This chapter describes the validation and verification of the developed modelling technology. This is done via its application to various benchmark problems found in literature.

- **Chapter 5**. **Summary, Conclusions and Recommendations for Future Work**. The final chapter summarises the contributions of the work done and makes recommendations for its continuation.

1.4 Publication List

Publications forthcoming from the research are as follow:

1.4.1 Journal Paper

Mowat, A. G. B., Malan, A. G., Van Zyl, L. H. and Meyer, J. P. (2011). A Hybrid Finite-Volume-ROM Approach to Non-Linear Aerospace Fluid-Structure Interaction Modelling, in progress.

1.4.2 Conference Paper

Mowat, A. G. B., Malan, A. G., Van Zyl, L. H. and Meyer, J. P. (2011). A Hybrid Finite-Volume-ROM Approach to Non-Linear Aerospace Fluid-Structure Interaction Modelling, In *Proceedings of the International Forum Aeroelasticity and Structural Dynamics* (IFASD2011), Paris, 26–30 June.

1.4.3 Technical Report

Malan, A. G., Mowat, A. G. B. and Oxtoby, O. F. (2011). A Unified Strongly Coupled Fluid-Structure-Interaction Methodology. *for European Union Framework Project 7*, **Deliverable D3.3**, 1–30.

Chapter 2

Governing Equations

2.1 Introduction

The fundamental aim of this project is to accurately model the flutter phenomenon of a flexible wing undergoing a non-linear response to aerodynamic forces resulting from sub- and transonic flow. Researchers [32, 33, 35, 36] in the field typically employ a subset of the Navier-Stokes equation set, namely the transient inviscid Euler equation set, for this purpose. This is, as the latter describes to sufficient accuracy, the lift and moment forces that dominate flutter at moderate angles of attack. In this chapter, these equations are detailed. In addition, the pitch-plunge equations that may represent the mechanics of a three-dimensional airfoil in two dimensions are described.

2.2 Fluid Governing Equations

As noted previously, for the purpose of this study, the transient inviscid Euler equation set was used to describe the compressible fluid domain as a continuum. Assuming that no chemical reactions occur in addition to the flow being convection dominated (negating buoyancy effects), the resulting equation set may be written for a two-dimensional ALE coordinate frame in the following non-dimensional conservative form

$$\frac{\partial \mathbf{U}}{\partial t} + \frac{\partial \mathbf{F}^j}{\partial x_j} = 0 \tag{2.1}$$

where t is time and the vector of flow variables $\mathbf{U}$ is

$$\mathbf{U} = \begin{pmatrix} \rho u_1 \\ \rho u_2 \\ \rho \\ \rho E \end{pmatrix} \tag{2.2}$$

Further, the ALE Eulerian flux vector $\mathbf{F}^j$ is

$$\mathbf{F}^j = \begin{pmatrix} w_j \rho u_1 + p\delta_{1j} \\ w_j \rho u_2 + p\delta_{2j} \\ w_j \rho \\ w_j \rho E + p u_j \end{pmatrix} \tag{2.3}$$

In this equation set, x_j is a fixed Eulerian Cartesian reference frame axis j, $w_j = u_j - v_j$ is the velocity relative to the moving reference frame, u_j is the fluid velocity, v_j is the moving reference frame velocity, ρ is the density, p is the pressure and E is the specific total energy of the fluid.

Equation (2.1) was cast into weak form by integrating over an arbitrary and moving volume $\mathcal{V}(t)$, with surface $\mathcal{S}(t)$, which is translated at velocity $\mathbf{v}$ as

$$\frac{\partial}{\partial t}\int_{\mathcal{V}(t)} \mathbf{U} d\mathcal{V} + \int_{\mathcal{S}(t)} \mathbf{F}^j n_j d\mathcal{S} = 0 \tag{2.4}$$

Note that in the above set of equations, the symbols were non-dimensionalised using free-stream conditions. Accordingly, non-dimensional quantities were related to their dimensional counter-parts (denoted by $*$) as follows

$$\begin{array}{cccc} t = \frac{t^* U^*_\infty}{L^*} & x_j = \frac{x^*_j}{L^*} & u_j = \frac{u^*_j}{U^*_\infty} & \rho = \frac{\rho^*}{\rho^*_\infty} \\ p = \frac{p^*}{(\rho^*_\infty U^{*2}_\infty)} & T = \frac{T^*}{(U^{*2}_\infty / C_p)} & E = \frac{E^*}{U^{*2}_\infty} & \end{array} \tag{2.5}$$

where ∞ denotes free stream, L is the characteristic length and T is the temperature. SI units of measurement were used for the dimensional quantities. Finally, C_p is specific heat at constant pressure.

2.2.1 Fluid Constitutive Equations

The governing equations were closed for the fluid domain via constitutive equations which relate density, pressure, temperature and acoustic velocity. For this purpose, the ideal gas law was assumed for this study, as for typical aerospace applications, the density is low relative to its critical point, viz.

$$p^* = \rho^* R T^* \tag{2.6}$$

where R is known as the gas constant which is defined as $R = C_p - C_v$, where C_v is the specific heat at constant volume.

The ratio of specific heats was assumed to be constant and was defined as

$$\gamma = \frac{C_p}{C_v} \tag{2.7}$$

which resulted in

$$R = C_p \frac{\gamma - 1}{\gamma} \tag{2.8}$$

If Equation (2.8) is substituted into Equation (2.6), the ideal gas law can be written in terms of the non-dimensional quantities as

$$\rho = \frac{p}{T}\frac{\gamma}{\gamma - 1} \tag{2.9}$$

The total specific energy is given by

$$E = \frac{p}{\rho(\gamma - 1)} + \frac{u_j u_j}{2} \tag{2.10}$$

where the first term on the right-hand side represents the internal energy and the second term the kinetic energy. The total specific enthalpy now follows as

$$H = E + \frac{p}{\rho} \tag{2.11}$$

Lastly, the acoustic velocity is defined in terms of dimensional quantities as

$$c^* = \sqrt{\frac{\gamma p^*}{\rho^*}} \tag{2.12}$$

and in terms of the non-dimensional variables as

$$c = \sqrt{\frac{\gamma p}{\rho}} \tag{2.13}$$

which results in $c = c^*/U^*_\infty$.

2.2.2 Fluid Boundary Conditions

In order to obtain a unique solution to the ALE Euler equations, appropriate boundary conditions had to be specified. In the absence of heat transfer from the airfoil surface, two boundary types were used in this study, viz. slip and characteristic boundary conditions. The former is applicable at solid wall boundaries, which implies that the velocity component of the flow normal to the boundary is set to the velocity of the moving boundary as

$$\mathbf{u} \cdot \mathbf{n} = \mathbf{v} \cdot \mathbf{n} \tag{2.14}$$

where the nomenclature is as defined previously.

Characteristic boundary conditions were employed at the far-field in order to avoid non-physical disturbance propagation. For the purpose of this study a sub-sonic altered characteristic-type analysis based on one-dimensional Riemann invariants (to determine which characteristics must enter or leave the domain) was employed [61, 62]. The Riemann invariants G were based on the free-stream and extrapolated values as

$$\begin{aligned} G_\infty &= \mathbf{u}_\infty \cdot \mathbf{n} - \tfrac{2c_\infty}{\gamma-1} \\ G_e &= \mathbf{u}_e \cdot \mathbf{n} - \tfrac{2c_e}{\gamma-1} \end{aligned} \tag{2.15}$$

where the subscript e denotes values determined by extrapolating the primitive variables. The acoustic velocities were defined as

$$\begin{aligned} c_\infty &= \sqrt{\frac{\gamma p_\infty}{\rho_\infty}} \\ c_e &= \sqrt{\frac{\gamma p_e}{\rho_e}} \end{aligned} \tag{2.16}$$

for which the acoustic velocity at the boundary could be written as

$$c_b = 0.25\,(\gamma - 1)\,(G_e - G_\infty) \tag{2.17}$$

The velocity magnitude normal to the boundary, then followed as

$$u_n = 0.5\,(G_e - G_\infty) \tag{2.18}$$

from which the velocity at the in- and outflow boundaries, respectively, could be calculated from

$$\mathbf{u}_b = \mathbf{u}_\infty + (u_n - \mathbf{u}_\infty \cdot \mathbf{n})\,\mathbf{n} \;\text{ and }\; \mathbf{u}_b = \mathbf{u}_e + (u_n - \mathbf{u}_e \cdot \mathbf{n})\,\mathbf{n} \tag{2.19}$$

The temperature at the in- and outflow boundaries, respectively, followed as

$$T_b = T_\infty \left(\frac{c_b^2}{c_\infty^2}\right) \;\text{ and }\; T_b = T_e \left(\frac{c_b^2}{c_e^2}\right) \tag{2.20}$$

and by applying the ideal-gas constant entropy relation, it followed that the pressure of the in- and outflow boundaries, respectively, were calculated as

$$p_b = p_\infty \left(\frac{T_b}{T_\infty}\right)^{\frac{\gamma}{\gamma-1}} \;\text{ and }\; p_b = p_e \left(\frac{T_b}{T_e}\right)^{\frac{\gamma}{\gamma-1}} \tag{2.21}$$

where the nomenclature is as defined previously.

2.3 Solid Governing Equations

For the purpose of this study the aeroelastic structural model is described by a two degrees-of-freedom pitch-plunge system, as shown in Figure 2.1. The equations of motion for this system are given by

$$\begin{aligned} m\ddot{h} + S_\alpha \ddot{\alpha} + K_h h &= -\mathrm{L} \\ S_\alpha \ddot{h} + I_\alpha \ddot{\alpha} + K_\alpha \alpha &= \mathrm{M}_\alpha \end{aligned} \tag{2.22}$$

where

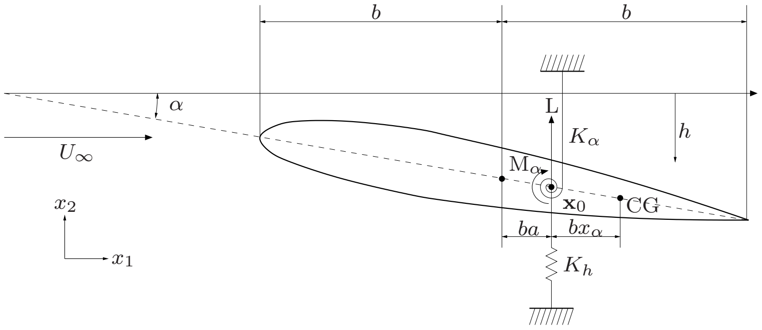

Figure 2.1: Schematic diagram of the airfoil pitch-plunge modal model. Here b denotes the semi-chord length, a denotes the position of the elastic centre measured from the mid-chord along the chord when the airfoil is at rest and x_α is the distance from the elastic centre to the centre of gravity (CG)

m :	mass of the airfoil per unit span
S_α :	static imbalance
I_α :	sectional moment of inertia of the airfoil
K_h :	plunging spring coefficient
K_α :	pitching spring coefficient
h :	vertical displacement (positive down)
α :	angle-of-attack
L :	sectional lift per unit span
M$_\alpha$:	sectional moment about the elastic centre (positive nose up).

and $\ddot{}$ quantities relate to second-derivatives with respect to time. The sectional lift and moment about the airfoil elastic centre were calculated as

$$\mathrm{L} = \int p n_2 d\mathcal{S} \quad \text{and} \quad \mathrm{M}_\alpha = \int (p n_j) \times \mathrm{r}_j d\mathcal{S} \tag{2.23}$$

where p denotes the pressure of the fluid on the surface $\mathcal{S}$ with outward pointing unit vector $\mathbf{n}$. Further, $\mathrm{r}_j = x_j - x_{0_j}$ is the distance from where the pressure is applied to the elastic centre, $\mathbf{x}_0$.

2.4 Conclusion

This chapter details the equations employed to describe the non-linear aeroelastic phenomena caused by sub- to transonic fluid flows. Both the fluid and structural domain were detailed, with the ALE formulation of the Euler equation set employed for the aforementioned. In the case of the structure, two degrees-of-freedom pitch-plunge equations were defined. The next chapter details the procedure employed to discretise and solve the complete system of equations in a fully coupled manner.

Chapter 3

Numerical Solution Procedure

3.1 Introduction

In this chapter, the numerical solution procedure is defined. This entails the spacial and temporal discretisation of both fluid and solid domains, as well as their fully coupled solution. The fluid is discretised spatially and temporally, while a ROM representation of the structure is employed.

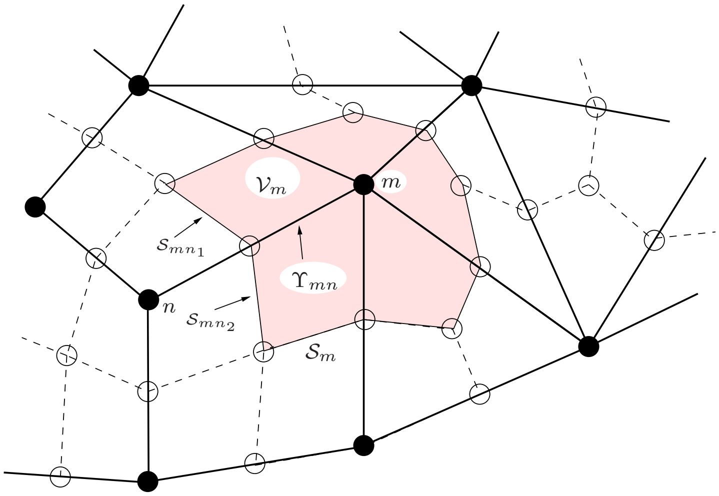

Figure 3.1: Schematic diagram of the construction of the median dual mesh on hybrid grids. Here, Υ_{mn} depicts the edge connecting nodes m and n

3.2 Fluid Spatial Discretisation

The discrete form of the surface integral in Equation (2.4), computed for the volume $\mathcal{V}_m$ (Figure 3.1) surrounding the node m, may be written as

$$\int_{\mathcal{S}_m(t)} \mathbf{F}^j n_j d\mathcal{S} \approx \sum_{\Upsilon_{mn} \cap \mathcal{V}_m(t)} \overline{\mathbf{F}^j}_{mn} \mathbf{C}^j_{mn} \tag{3.1}$$

where all $\overline{\bullet}_{mn}$ quantities denote edge-face values.

The above equation employs a vertex-centred edge-based finite volume algorithm [63, 64] for the purposes of spatial discretisation of the fluid domain. This algorithm was selected as it allows natural generic mesh applicability, second-order accuracy without odd-even decoupling, and computational efficiency which is factors greater than element-based approaches [65]. Note that the proposed edge-based approach is also particularly well suited to shared memory parallel computing.

Surface integrals were calculated in an edge-wise manner and, for this purpose, bounding surface information was similarly stored in an edge-wise manner, termed *edge-coefficients*. For a given internal edge, Υ_{mn} connecting nodes m and n, edge-coefficients are defined as a function of time, i.e.

$$\mathbf{C}_{mn}(t) = \mathbf{n}^{mn_1}\mathcal{S}_{mn_1}(t) + \mathbf{n}^{mn_2}\mathcal{S}_{mn_2}(t) = \mathbf{n}^{mn}\mathcal{S}_{mn}(t) \tag{3.2}$$

where $\mathcal{S}_{mn_1}$ is a bounding surface-segment intersecting the edge (Figure 3.1) and the normal unit vectors were similarly a function of time.

For the purpose of calculating the edge-face flux values, $\overline{\mathbf{F}^j}_{mn}$, three schemes are considered and compared, viz. Roe, HLLC and AUSM$^+$-up schemes. In all cases, the second order MUSCL scheme with van Albada limiter function was employed to interpolate the left and right states, as detailed below.

MUSCL scheme

A limited second order MUSCL scheme [66] for unstructured meshes was used to calculate the left and right states, as required in each of the employed upwind methods. The left and right states were defined as

$$\begin{aligned} \phi^L_{mn} &= \phi_m + \tfrac{1}{2}\psi\left(r^L_{mn}\right)\left(2\nabla\phi_m - \Delta^+_m\right) \\ \phi^R_{mn} &= \phi_n - \tfrac{1}{2}\psi\left(r^R_{mn}\right)\left(2\nabla\phi_n - \Delta^+_m\right) \end{aligned} \tag{3.3}$$

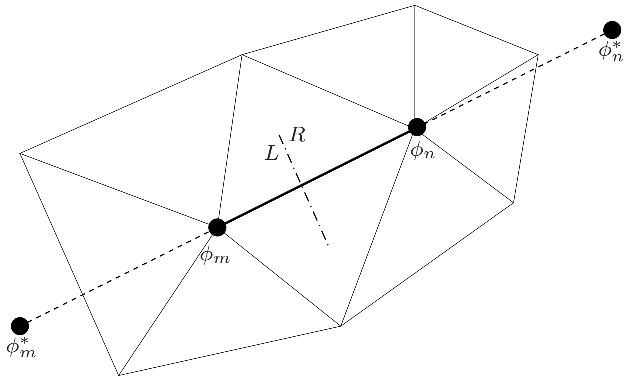

Figure 3.2: Schematic diagram of an unstructured mesh illustrating the position of ϕ_m^* and ϕ_n^* for the MUSCL formulation

where, $\nabla\phi$ is the computed gradient and ψ is the van Albada limiter [58], and

$$\begin{aligned}
\Delta_m^+ &= \phi_n - \phi_m \\
\Delta_m^- &= \phi_m - \phi_m^* = 2\nabla\phi_m - (\phi_n - \phi_m) \\
&= 2\nabla\phi_m - \Delta_m^+ \\
\Delta_n^+ &= \phi_n^* - \phi_n = 2\nabla\phi_n - (\phi_n - \phi_m) \\
&= 2\nabla\phi_n - \Delta_m^+
\end{aligned} \tag{3.4}$$

In Equation (3.4), the ϕ^* quantities denote upwind and downwind extrapolated values, as in Figure 3.2, and

$$\psi(r) = \frac{r(r+1)}{r^2+1} \tag{3.5}$$

with

$$\begin{aligned}
r_{mn}^L &= \frac{\Delta_m^-}{\Delta_m^+} = \frac{2\nabla\phi_m - \Delta_m^+}{\Delta_m^+} \\
r_{mn}^R &= \frac{\Delta_n^-}{\Delta_m^+} = \frac{2\nabla\phi_n - \Delta_m^+}{\Delta_m^+}
\end{aligned}$$

where the nomenclature is as defined previously.

For the chosen upwind schemes, viz. Roe, HLLC and AUSM$^+$-up, the ALE formulations for the unstructured edged-based approach is detailed next.

Roe Scheme

The Roe scheme is widely used and is thus a well-established upwind scheme. This is due to its ability to accurately resolve the boundary layer and good resolution of shocks. The ALE Roe flux was defined as follows [67–69]

$$\overline{\mathbf{F}^j}_{mn} = \tfrac{1}{2}\left[\mathbf{F}^j(\mathbf{U}_L) + \mathbf{F}^j(\mathbf{U}_R)\right] - \tfrac{1}{2}\sum_{i=1}^{4} |\hat{\lambda}_i^j| \hat{\alpha}_i^j \hat{\mathbf{K}}_i^j \tag{3.6}$$

where the $\mathbf{F}^j()$ quantities denote left and right states (calculated via second-order MUSCL) and the summation term contains eigenvalue/eigenvector information. The computation of the latter commences by calculating the Roe averages, which requires computation of the ratio, $\hat{R}$, of the left and right density as

$$\hat{R} = \sqrt{\frac{\rho_R}{\rho_L}} \tag{3.7}$$

Once $\hat{R}$ was determined, the Roe-averaged density, velocity, specific enthalpy and acoustic velocity could be calculated as follows:

$$\hat{\rho} = \hat{R}\rho_L \tag{3.8}$$

$$\hat{u}_j = \frac{\hat{R}u_{R_j} + u_{L_j}}{\hat{R}+1} \tag{3.9}$$

$$\hat{H} = \frac{\hat{R}H_R + H_L}{\hat{R}+1} \tag{3.10}$$

$$\hat{c} = \sqrt{(\gamma - 1)(\hat{H} - \tfrac{1}{2}[\hat{u}_1^2 + \hat{u}_2^2])} \tag{3.11}$$

The eigenvalues of the Jacobian for the ALE formulation are given by

$$\hat{\lambda}_1^j = \hat{u}_j - v_j \qquad \hat{\lambda}_2^j = \hat{u}_j - v_j \qquad \hat{\lambda}_3^j = \hat{u}_j - \hat{c} - v_j \qquad \hat{\lambda}_4^j = \hat{u}_j + \hat{c} - v_j \tag{3.12}$$

with the eigenvectors being

$$\hat{\mathbf{K}}_1^j = \begin{pmatrix} \delta_{1j}\hat{u}_1 + \delta_{2j} \\ \delta_{1j}\hat{u}_2 \\ \delta_{1j} \\ \delta_{1j}\tfrac{1}{2}[\hat{u}_1^2 + \hat{u}_2^2] + \delta_{2j}\hat{u}_1 \end{pmatrix} \quad \hat{\mathbf{K}}_2^j = \begin{pmatrix} \delta_{2j}\hat{u}_1 \\ \delta_{2j}\hat{u}_2 + \delta_{1j} \\ \delta_{2j} \\ \delta_{2j}\tfrac{1}{2}[\hat{u}_1^2 + \hat{u}_2^2] + \delta_{1j}\hat{u}_2 \end{pmatrix}$$

$$\hat{\mathbf{K}}_3^j = \begin{pmatrix} \hat{u}_1 - \delta_{1j}\hat{c} \\ \hat{u}_2 - \delta_{2j}\hat{c} \\ 1 \\ \hat{H} - (\delta_{1j}\hat{u}_1 + \delta_{2j}\hat{u}_2)\hat{c} \end{pmatrix} \quad \hat{\mathbf{K}}_4^j = \begin{pmatrix} \hat{u}_1 + \delta_{1j}\hat{c} \\ \hat{u}_2 + \delta_{2j}\hat{c} \\ 1 \\ \hat{H} + (\delta_{1j}\hat{u}_1 + \delta_{2j}\hat{u}_2)\hat{c} \end{pmatrix} \tag{3.13}$$

Finally, the wave strengths, $\hat{\alpha}$, were defined as

$$\hat{\alpha}_1^j = \left(\Delta\rho - \frac{1}{\hat{c}^2}\Delta p\right)\delta_1 j + (\hat{\rho}\Delta u_1)\,\delta_2 j \tag{3.14}$$

$$\hat{\alpha}_2^j = \left(\Delta\rho - \frac{1}{\hat{c}^2}\Delta p\right)\delta_2 j + (\hat{\rho}\Delta u_2)\,\delta_1 j \tag{3.15}$$

$$\hat{\alpha}_3^j = \frac{1}{2\hat{c}^2}(\Delta p - \hat{\rho}\hat{c}\Delta u_j) \tag{3.16}$$

$$\hat{\alpha}_4^j = \frac{1}{2\hat{c}^2}(\Delta p + \hat{\rho}\hat{c}\Delta u_j) \tag{3.17}$$

where $\Delta(\cdot) = (\cdot)_R - (\cdot)_L$.

The above Roe scheme is problematic when used to resolve transonic rarefaction waves, as is the case in certain shock tube problems. However, this deficiency was addressed by Harten and Hyman [70] where the left and right non-linear waves associated with the respective eigenvalues $\hat{\lambda}_3^j = \hat{u}_j - \hat{c} - v_j$ and $\hat{\lambda}_4^j = \hat{u}_j + \hat{c} - v_j$ were modified. In terms of aeroelastic cases, this deficiency is, however typically, not relevant.

HLLC Scheme

The HLLC scheme [48, 71] is a more recent development compared to Roe, and has similar computational cost. The method resolves the shock and contact waves exactly and is positively conservative. The HLLC flux is defined as

$$\overline{\mathbf{F}^j}_{mn} = \begin{cases} \mathbf{F}_L^j & \text{if} \quad S_L > 0 \\ \mathbf{F}^j(\mathbf{U}_L^\star) & \text{if} \quad S_L \leq 0 < S_M \\ \mathbf{F}^j(\mathbf{U}_R^\star) & \text{if} \quad S_M \leq 0 \leq S_R \\ \mathbf{F}_R^j & \text{if} \quad S_R < 0 \end{cases} \tag{3.18}$$

where

$$\mathbf{F}^j(\mathbf{U}_{L/R}^\star) = \begin{pmatrix} S_M(\rho u_1)^\star + p^\star\delta_{1j} \\ S_M(\rho u_2)^\star + p^\star\delta_{2j} \\ S_M\rho^\star \\ S_M(\rho E)^\star + (S_M + v_j)p^\star \end{pmatrix}_{L/R} \tag{3.19}$$

and

$$\begin{pmatrix} (\rho u_1)^\star \\ (\rho u_2)^\star \\ \rho^\star \\ (\rho E)^\star \end{pmatrix}_{L/R} = \frac{1}{S_{L/R} - S_M} \begin{pmatrix} (S-w)(\rho u_1) + (p^\star - p)\delta_{1j} \\ (S-w)(\rho u_2) + (p^\star - p)\delta_{2j} \\ (S-w)\rho \\ (S-w)(\rho E) - pw + p^\star S_M \end{pmatrix}_{L/R} \tag{3.20}$$

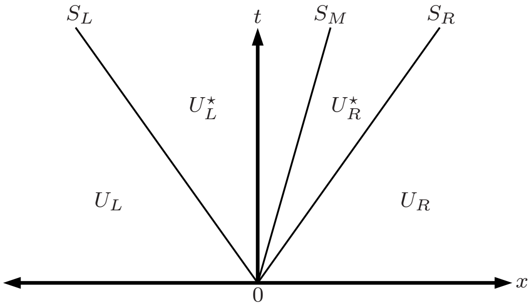

Figure 3.3: Diagram showing the HLLC Riemann Solver and how the wave speeds, S_L, S_M and S_R, separate the different regions

Here $(\cdot)_{L/R}$ quantities denote the left or right states of that particular variable, respectively. Further,

$$p^\star = \rho_L(w_L - S_L)(w_L - S_M) + p_L = \rho_R(w_R - S_R)(w_R - S_M) + p_R \quad (3.21)$$

where $w = (\mathbf{u} - \mathbf{v}) \cdot \mathbf{n}$ is the relative velocity and $\mathbf{n}$ is the volume-face outward pointing normal unit vector.

The wave speeds, S_M, S_L and S_R, as shown in Figure 3.3, are defined as

$$S_M = \frac{\rho_R w_R(S_R - w_R) - \rho_L w_L(S_L - w_L) + p_L - p_R}{\rho_R(S_R - w_R) - \rho_L(S_L - w_L)} \quad (3.22)$$

where

$$S_L = \min[w_L - c_L, (\hat{\mathbf{u}} - \mathbf{v}) \cdot \mathbf{n} - \hat{c}] \quad (3.23)$$

and

$$S_R = \max[w_R + c_R, (\hat{\mathbf{u}} - \mathbf{v}) \cdot \mathbf{n} + \hat{c}] \quad (3.24)$$

Here $\hat{\mathbf{u}}$ and $\hat{c}$ are the Roe averages for the velocity vector and the acoustic speed respectively, which are a function of the left and right states.

AUSM$^+$-up Scheme

The AUSM$^+$-up scheme [42] is the latest development in the AUSM family [40, 41] of schemes and, as such, constitutes the most modern of the schemes employed in this study. The -up scheme is an improvement on its predecessors in terms of robustness and convergence rate. For the AUSM$^+$-up scheme, the ALE Eulerian flux vector $\mathbf{F}^j$ is written as

$$\mathbf{F}^j = \begin{pmatrix} w_j \rho u_1 + p\delta_{1j} \\ w_j \rho u_2 + p\delta_{2j} \\ w_j \rho \\ w_j \rho H + p v_j \end{pmatrix} \quad (3.25)$$

The AUSM$^+$-up scheme recognises the difference between the convection and pressure fluxes and thus treats them independently as

$$\overline{\mathbf{F}^j}_{mn} = \dot{m}_{mn}\vec{\psi}_{mn} + \mathbf{p}_{mn_j} \tag{3.26}$$

with

$$\vec{\psi}_{mn} = \begin{cases} \vec{\psi}_L & \text{if} \quad \dot{m}_{mn} > 0 \\ \vec{\psi}_R & \text{otherwise} \end{cases} \qquad \text{where} \quad \vec{\psi} = \begin{pmatrix} u_1 \\ u_2 \\ 1 \\ \rho H \end{pmatrix} \tag{3.27}$$

and

$$\mathbf{p}_{mn_j} = \begin{pmatrix} p\delta_{1j} \\ p\delta_{1j} \\ 0 \\ pv_j \end{pmatrix}_{mn} \tag{3.28}$$

To calculate $\dot{m}_{mn}$ and p_{mn}, the relative Mach number at the interface between the left and the right state was defined with

$$M_L = \frac{w_L}{c_{mn}} \qquad \text{and} \qquad M_R = \frac{w_R}{c_{mn}} \tag{3.29}$$

where $w = (\mathbf{u} - \mathbf{v}) \cdot \mathbf{n}$ is the relative velocity for the left and right states as defined previously. Numerous expressions are in use to calculate c_{mn} [42]. In this study we employed

$$c_{mn} = \min\left(c_L, c_R\right) \tag{3.30}$$

where

$$c_L = \frac{\tilde{c}^2}{\max(\tilde{c}, w_L)} \qquad c_R = \frac{\tilde{c}^2}{\max(\tilde{c}, -w_R)} \tag{3.31}$$

In Equation (3.31), $\tilde{c}$ is the critical acoustic velocity which, for an ideal gas, can be expressed in terms of total enthalpy as

$$\tilde{c}^2 = \frac{2\left(\gamma - 1\right)}{\gamma + 1} H \tag{3.32}$$

The mean local Mach number was used

$$\overline{M}^2 = \frac{w_L^2 + w_R^2}{2c_{mn}^2} \tag{3.33}$$

to determine a reference Mach number

$$M_o^2 = \min\left(1, \max\left(\overline{M}^2, M_\infty^2\right)\right) \;\in\; [0, 1] \tag{3.34}$$

where M_∞ is the free-stream value. The reference Mach number was ultimately used to calculate a scaling factor

$$f_a\left(M_o\right) = M_o\left(2 - M_o\right) \quad \in \quad [0,1] \tag{3.35}$$

To calculate the mass flux at the interface, the split Mach number function was defined as

$$\mathcal{M}^{\pm}(M) = \begin{cases} \frac{1}{2}(M \pm |M|) & \text{if} \quad |M| \geq 1 \\ \mathcal{M}^{\pm}_{\beta}(M) & \text{otherwise} \end{cases} \tag{3.36}$$

where

$$\mathcal{M}^{\pm}_{\beta} = \pm\tfrac{1}{4}(M \pm 1)^2 \pm \beta(M^2 - 1)^2 \quad -\tfrac{1}{16} \leq \beta \leq \tfrac{1}{2} \tag{3.37}$$

and for the purpose of this study, $\beta = \frac{1}{8}$ was used. Next, the Mach number at the interface was

$$M_{mn} = \mathcal{M}^{+}(M_L) + \mathcal{M}^{-}(M_R) + M_p \tag{3.38}$$

where

$$M_p = -K_p \max(1 - \sigma\overline{M}^2, 0)\frac{p_R - p_L}{0.5(\rho_L + \rho_R)c^2_{mn}} \tag{3.39}$$

and the constants were defined as $0 \leq K_p \leq 1$ and $\sigma \leq 1$. In this study, $K_p = 0.25$ and $\sigma = 1$ [42] was set. The mass flux was defined as

$$\dot{m}_{mn} = c_{mn}M_{mn}\begin{cases} \rho_L & \text{if } M_{mn} > 0 \\ \rho_R & \text{otherwise} \end{cases} \tag{3.40}$$

Considering p_{mn} next, the split pressure function was

$$\mathcal{P}^{\pm}(M) = \begin{cases} \frac{1}{2}(1 \pm \text{sign}(M)) & \text{if} \quad |M| \geq 1 \\ \mathcal{P}^{\pm}_{\tilde{\alpha}}(M) & \text{otherwise} \end{cases} \tag{3.41}$$

where

$$\mathcal{P}^{\pm}_{\tilde{\alpha}} = \tfrac{1}{4}(M \pm 1)^2(2 \mp M) \pm \tilde{\alpha}M(M^2 - 1)^2, \quad -\tfrac{3}{4} \leq \tilde{\alpha} \leq \tfrac{3}{16} \tag{3.42}$$

and

$$\tilde{\alpha} = \frac{3}{16}\left(-4 + 5f_a^2\right) \tag{3.43}$$

The pressure flux could be written as

$$p_{mn} = \mathcal{P}^{+}p_L + \mathcal{P}^{-}p_R - K_u\mathcal{P}^{+}\mathcal{P}^{-}(\rho_L + \rho_R)c_{mn}(w_R - w_L) \tag{3.44}$$

where $\mathcal{P}^{+} = \mathcal{P}^{+}(M_L)$, $\mathcal{P}^{-} = \mathcal{P}^{-}(M_R)$ and $0 \leq K_u \leq 1$. For the purpose of this study $K_u = 0.75$ [42] was set. The above scheme may appear the most computationally intensive of the three considered. However, it does not contain square root computations, resulting in an efficient method.

3.3 Fluid Temporal Discretisation

For the purpose of describing temporal discretisation the fluid governing equation (2.4) may be written in semi-discrete form as

$$\frac{dU_i}{dt} = -\int_{\mathcal{S}(t)} F_i^j n_j dS \tag{3.45}$$

where $i = 1 \ldots 4$. Dual-time-stepping [64] was employed for real time discretisation as

$$\frac{\Delta U_i}{\Delta t_\tau} V^\tau = -\int_{\mathcal{S}(t)} F_i^j n_j dS \bigg|^\tau + \mathbf{S}^\tau V^\tau = \mathbf{R}_i(\mathbf{U}^{n+1}) V^\tau \tag{3.46}$$

where the τ superscript denotes the latest (existing) solution or pseudo-timestep and $\Delta t_\tau = t^{\tau+1} - t^\tau$. The source term $\mathbf{S}$ constitutes a second-order backward difference method

$$\mathbf{S}^\tau V^\tau = -\frac{3\mathbf{U}^\tau V^\tau - 4\mathbf{U}^n V^n + \mathbf{U}^{n-1} V^{n-1}}{2\Delta t} \tag{3.47}$$

where Δt denotes the real-timestep-size, the n superscript is the existing real-timestep and the timestep being solved for is $n+1$.

The fourth-order Runge-Kutta solution method then followed as

$$\begin{aligned} &\mathbf{U}_m^{(0)} = \mathbf{U}_m^\tau \\ &\mathbf{U}_m^{(k)} = \mathbf{U}_m^{(0)} + \kappa_k \Delta t^\tau \mathbf{R}_m^{k-1} \;\text{ for }\; k = 1 \;\text{ to }\; 3 \\ &\mathbf{U}_m^{(\tau+1)} = \mathbf{U}_m^4 \end{aligned} \tag{3.48}$$

where the coefficients κ_k are 0.11, 0.2766 and 0.5 as defined by Lallemand *et al.* [72]. The pseudo-timestep local to each computational cell was determined in the interest of optimal convergence, while ensuring a stable solution process. To this end, the following expression was employed

$$\Delta t_\tau = \mathrm{CFL} \left[\frac{|u_j - v_j| + c}{\Delta x_j} \right]^{-1} \tag{3.49}$$

where CFL denotes the Courant-Friedrichs-Lewy number and Δx_j is the effective mesh spacing in direction j.

3.4 Geometric Conservation Law

The Geometric Conservation Law (GCL) requires that the numerical scheme chosen to solve the fluid equations and the algorithm employed to update the mesh position must preserve the trivial solution of a uniform flow field in the presence of a moving mesh [35, 73]. This implies that no erroneous fluxes are introduced by the movement of an edge when the control volume is deformed. The GCL conditions were applied to Equation (3.46) by satisfying

$$\frac{\partial V}{\partial t} - \int_{d\mathcal{S}(t)} \mathbf{v} \cdot \mathbf{n} d\mathcal{S} = 0 \tag{3.50}$$

This equation was discretised to obtain the latest cell volume by a second order backward difference scheme as

$$\left(\frac{\frac{3}{2}V^{n} - 2V^{n-1} + \frac{1}{2}V^{n-2}}{\Delta t} \right) - \sum_{i=1}^{n_{edge}} v_{mn_i} C_{mn_i} = 0 \tag{3.51}$$

The above equation implies that the change in area of the control volume, $\mathcal{V}$, is discretely equal to the swept area of its bounding edges, thus satisfying the geometric conservation law. In this study a second-order interpolation scheme was employed to calculate the edge velocity, v_{mn_i}.

3.5 Solid Solution Procedure

Considering the structure system next, the non-dimensional form of the modal response to Equation (2.22) may be written as

$$[\mathbf{M}]\{\ddot{\mathbf{q}}\} + [\mathbf{K}]\{\mathbf{q}\} = \{\mathbf{Q}\} \tag{3.52}$$

where, as before, $\ddot{}$ quantities denote second-derivatives with respect to time. Here, the non-dimensional mass matrix, stiffness matrix and displacement vectors are defined as

$$\mathbf{M} = \begin{bmatrix} 1 & x_\alpha \\ x_\alpha & r_\alpha^2 \end{bmatrix}; \quad \mathbf{K} = \begin{bmatrix} \left(\frac{\omega_h}{\omega_\alpha}\right)^2 & 0 \\ 0 & r_\alpha^2 \end{bmatrix}; \quad \mathbf{q} = \left\{ \begin{array}{c} \frac{h}{b} \\ \alpha \end{array} \right\} \tag{3.53}$$

where x_α and r_α^2 denote structural parameters defined as $\frac{S_\alpha}{mb}$ and $\frac{I_\alpha}{mb^2}$, respectively. Further, ω_h and ω_α are the uncoupled natural frequencies of plunge and pitch, respectively. The definition of the generalised force vector, $\mathbf{Q}$, will be defined later in the chapter.

The reduced frequency, k_c, is typically written in terms of the flutter speed, V_f, as

$$k_c = \frac{\omega_\alpha \mathrm{c}}{2U_\infty} = \frac{1}{V_f \sqrt{\mu}} \tag{3.54}$$

where c is the chord length of the airfoil, U_∞ is the free-stream velocity and μ denotes the airfoil mass ratio, defined as $\mu = \frac{m}{\pi \rho b^2}$. The flutter speed, V_f, is defined as

$$V_f = \frac{U_\infty}{\omega_\alpha b \sqrt{\mu}} \tag{3.55}$$

The non-dimensional ROM Equation (3.52) may be cast in a manner suitable for solution as

$$\dot{\mathbf{r}} = [\Psi]\,\mathbf{r} + \{\Phi\} \tag{3.56}$$

where the state vector $\mathbf{r} = \{\mathbf{r}_1, \mathbf{r}_2\}$, with $\mathbf{r}_1 = \{h/b, \alpha\}$ and $\mathbf{r}_2 = \dot{\mathbf{r}}_1$. Further

$$\Psi = \begin{bmatrix} 0 & [\mathbf{I}] \\ -[\mathbf{M}]^{-1}[\mathbf{K}] & 0 \end{bmatrix}; \quad \Phi = \begin{Bmatrix} 0 \\ [\mathbf{M}]^{-1}\{\mathbf{Q}\} \end{Bmatrix} \tag{3.57}$$

The generalised force vector, $\mathbf{Q}$, may be calculated for the general case as

$$Q_k = \sum_{i}^{nodes} \mathbf{f}^i \cdot \frac{d\mathbf{x}^i}{dr_{1_k}} \tag{3.58}$$

where $\mathbf{x}^i$ and $\mathbf{f}^i$, respectively, denote the displaced coordinate and aerodynamic force at node i on the airfoil surface. The manner in which $\mathbf{x}^i$ is related to the state vector, $\mathbf{r}$, determines the type of ROM which results. In the 2D pitch-plunge case, the following analytical expression may be employed

$$\begin{bmatrix} x_1 \\ x_2 \end{bmatrix} = \begin{Bmatrix} \cos\alpha & -\sin\alpha \\ \sin\alpha & \cos\alpha \end{Bmatrix} \begin{bmatrix} x_{r_1} - x_{0_1} \\ x_{r_2} - x_{0_2} \end{bmatrix} + \begin{bmatrix} x_{0_1} \\ x_{0_2} - h \end{bmatrix} \tag{3.59}$$

where x_{r_j} is the initial coordinate of the surface and x_{0_j} is the coordinate of the airfoil elastic axis at rest, that is $\alpha = 0$. To obtain the generalised force the lift and moment was non-dimensionalise into the lift and moment coefficient as

$$C_{\mathrm{L}} = \frac{\mathrm{L}}{\rho_\infty^* U_\infty^{*2} b} \qquad C_{\mathrm{M}} = \frac{\mathrm{M}_\alpha}{2\rho_\infty^* U_\infty^{*2} b^2} \tag{3.60}$$

where nomenclature is as previously defined. The generalised force is given as

$$\mathbf{Q} = \frac{1}{\pi \mu k_c^2} \begin{Bmatrix} -C_l \\ 2C_m \end{Bmatrix} \tag{3.61}$$

However, when considering extension to three dimensions, an analytical expression such as Equation (3.59) is typically not easily available, making the linear modal approximation considerably more convenient, viz.

$$\mathbf{x}^i = \mathbf{x}_r^i + \sum_{k}^{modes} \mathbf{r}_{1_k} \hat{\mathbf{u}}_k^i \tag{3.62}$$

where $\hat{\mathbf{u}}$ is a normalised linear mode shape (eigenvector) which for the two-dimensional pitch-plunge case, was $\hat{\mathbf{u}}_1 = (0, -b)$ and $\hat{\mathbf{u}}_2 = (x_{r_2} - x_{0_2}, x_{0_1} - x_{r_1})$. This resulted in the following linear expression for the generalised force vector:

$$\hat{Q}_k = \sum_{i}^{nodes} \mathbf{f}^i \cdot \hat{\mathbf{u}}_k^i \tag{3.63}$$

where

$$\mathbf{f}^i = \frac{p_i \mathbf{n}}{\rho_\infty^* U_\infty^{*2} b} \tag{3.64}$$

is the non-dimensionalised aerodynamic force at node i. In this study however, the accuracy of the linear ROM is improved upon via the use of a so-called *quadratic* [54] extension, viz.

$$\mathbf{x}^i = \mathbf{x}_r^i + \sum_k^{modes} \mathbf{r}_{1_k} \hat{\mathbf{u}}_k^i + \sum_k^{modes} \sum_l^{modes} \mathbf{r}_{1_k} \mathbf{r}_{1_l} \hat{\mathbf{g}}_{kl}^i \tag{3.65}$$

which resulted in no significant additional FSI computational cost. The resulting generalised force expression reads

$$\hat{Q}_k = \sum_i^{nodes} \mathbf{f}^i \cdot \hat{\mathbf{u}}_k^i + \sum_i^{nodes} \sum_l^{modes} 2\mathbf{r}_{1_l} \mathbf{f}^i \cdot \hat{\mathbf{g}}_{kl}^i \tag{3.66}$$

where the normalised quadratic mode shapes for the 2D pitch-plunge case are

$$\begin{aligned} \hat{\mathbf{g}}_{11} &= (0, \;\; 0) & \hat{\mathbf{g}}_{12} &= (0, \;\; 0) \\ \hat{\mathbf{g}}_{21} &= (0, \;\; 0) & \hat{\mathbf{g}}_{22} &= \left(\tfrac{x_{0_1} - x_{r_1}}{2}, \;\; \tfrac{x_{0_2} - x_{r_2}}{2} \right) \end{aligned} \tag{3.67}$$

In the case of the linear and quadratic ROMs, the generalised forces were similarly normalised as

$$\mathbf{Q} = \frac{1}{\pi \mu k_c^2} \left\{ \begin{array}{c} \frac{\hat{Q}_1}{b} \\ 2\hat{Q}_2 \end{array} \right\} \tag{3.68}$$

The above, resulted in an initial value problem, for which the spatial accuracy depended on whether the semi-analytical, linear or quadratic expressions were employed.

Note that the above expressions are written in non-dimensional structural time, $\Delta\tau_s$. This relates to the fluid non-dimensional time, i.e. $\Delta\tau_s = 2k_c\Delta t$. The resulting initial value problem was solved accurately via a fourth-order Runge-Kutta method as follows:

$$\mathbf{r}_k^{n+1} = \mathbf{r}_k^n + \tfrac{1}{6}\left(\kappa_{1k} + 2\kappa_{2k} + 2\kappa_{3k} + \kappa_{4k}\right) \tag{3.69}$$

where $k = 1, 2$ relating to $\mathbf{r}_1$ and $\mathbf{r}_2$ in Equation (3.56) and $\mathtt{h} = \tau_s^{n+1} - \tau_s^n$

was the timestep size. The κ values were defined as

$$\begin{aligned}
\kappa_{11} &= \mathtt{h}\{\mathbf{r}_2^n\} \\
\kappa_{12} &= \mathtt{h}\left(-\left[\mathbf{M}\right]^{-1}\left[\mathbf{K}\right]\{\mathbf{r}_1^n\} + \left[\mathbf{M}\right]^{-1}\{\mathbf{Q}^n\}\right) \\
\kappa_{21} &= \mathtt{h}\{\mathbf{r}_2^n + \tfrac{1}{2}\kappa_{12}\} \\
\kappa_{22} &= \mathtt{h}\left(-\left[\mathbf{M}\right]^{-1}\left[\mathbf{K}\right]\{\mathbf{r}_1^n + \tfrac{1}{2}\kappa_{11}\} + \left[\mathbf{M}\right]^{-1}\{\mathbf{Q}^{n+1/2}\}\right) \\
\kappa_{31} &= \mathtt{h}\{\mathbf{r}_2^n + \tfrac{1}{2}\kappa_{22}\} \\
\kappa_{32} &= \mathtt{h}\left(-\left[\mathbf{M}\right]^{-1}\left[\mathbf{K}\right]\{\mathbf{r}_1^n + \tfrac{1}{2}\kappa_{21}\} + \left[\mathbf{M}\right]^{-1}\{\mathbf{Q}^{n+1/2}\}\right) \\
\kappa_{41} &= \mathtt{h}\{\mathbf{r}_2^n + \kappa_{32}\} \\
\kappa_{42} &= \mathtt{h}\left(-\left[\mathbf{M}\right]^{-1}\left[\mathbf{K}\right]\{\mathbf{r}_1^n + \kappa_{31}\} + \left[\mathbf{M}\right]^{-1}\{\mathbf{Q}^{n+1}\}\right)
\end{aligned} \tag{3.70}$$

where $\mathbf{Q}^{n+1/2}$ was calculated using fourth-order Lagrange polynomials, based on the generalised forces at timesteps $n+1$, n, $n-1$ and $n-2$.

3.6 Fluid-solid Interface Treatment

At the fluid-solid interface, the following equations for traction, displacement and velocity are prescribed:

$$\begin{aligned}
(p_f)\, n_j &= -\,(p_s)\, n_j \\
\mathbf{u}_f &= \mathbf{v}_s \\
\mathbf{x}_f &= \mathbf{x}_s
\end{aligned} \tag{3.71}$$

where the subscripts f and s, respectively, denote fluid and solid interface and n_j is the related outward pointing normal unit vector. The above are prescribed as part of the pseudo-stepping iterative procedure.

3.7 FSI Solution and Dynamic Mesh Movement

For the purpose of simultaneous solution of the discretised fluid-solid equations in a manner which effects strong coupling, stability and computational efficiency, the following solution sequence was employed in an iterative fashion:

1. The fluid and solid discrete equations were solved via a single iteration of Equations (3.48) and (3.70), respectively.
2. Next, the calculated fluid tractions were applied to the solid boundary, and the calculated solid velocity and displacement to the fluid.

3. The above was repeated until the displacement of a solid mesh boundary node exceeded 30% of the element size or the residual of the fluid was reduced by two orders of magnitude (a real-timestep is considered converged when the residual of both the fluid and solid equations has dropped by at least three orders of magnitude).

4. The solid and fluid meshes were moved. In the case of the latter, non-boundary nodes were re-positioned via the mesh movement algorithm outlined below. The fluid mesh boundary velocities were calculated to second-order accuracy.

5. The residuals were then calculated for all equations and if larger than the convergence tolerance, steps 1 through 4 were repeated.

6. If the residuals were below the convergence tolerance, the real-timestep was terminated, and the next timestep entered into by proceeding to step 1. The procedure was started from projected estimates for spatial location and velocity (via second-order extrapolation) in the interest of convergence speed.

In FSI calculations, mesh movement based on optimisation of mesh quality [74] or on spring-damper systems is typically used [75]. To solve these systems, which have as many unknowns as the flow calculations, typically takes a substantial fraction of the simulation time – in many cases as much as 40% of total computation time [76]. However, such approaches are not warranted when displacements are comparatively small.

In light of the above, a simple and efficient interpolation scheme which is well suited to parallel computing [76] was employed for this study. Here, an internal node was moved as a function of the displacement of the closest two boundary points (identified at the start of the simulation) as follows:

$$\delta \mathbf{x} = \mathtt{r}_b \delta \mathbf{x}_1 + (1 - \mathtt{r}_b)\delta \mathbf{x}_2 \tag{3.72}$$

where $\delta \mathbf{x}_1$ and $\delta \mathbf{x}_2$ are, respectively, the displacements of the closest internal and external boundary points and $\mathtt{r}_b$, which varies between zero and one, was computed as

$$\mathtt{r}_b = \frac{D_2^{\mathtt{a}}}{D_1^{\mathtt{a}} + D_2^{\mathtt{a}}} \text{ with } \mathtt{a} = 3/2 \tag{3.73}$$

Here D_1 and D_2 denote the distances to the identified boundary points. Since the closest points and the values of $\mathtt{r}_b$ were calculated only once at the beginning of the analysis, the application of the mesh movement function was essentially instantaneous, and the mesh did not deteriorate due to repeated oscillations.

3.8 Parallel Computing

FSI simulations are computationally intensive due to the large number of timesteps involved. Making use of parallel computing was therefore of significant value. Because of the fully matrix-free nature of the numerical method at solver sub-iteration level, data reference was local (nodes only see neighbouring nodes, with some exceptions), which means that computation could be efficiently parallelised. To this end, the mesh may be divided into separate domains by applying the METIS library [77] to its connectivity graph. As far as the solver is concerned, the 'MPICH' MPI library was employed to transfer the data between domains [78].

3.9 Conclusion

In this chapter, the employed partitioned coupled FSI solution procedure was detailed. In the case of the fluid, an edge-based vertex-centred finite volume algorithm for spacial discretisation was employed along with a dual-timestepping method for temporal discretisation. The three chosen upwind schemes were detailed. In the case of the solid, the semi-analytical, linear and quadratic ROM formulation were detailed, including the fourth-order Runge-Kutta method employed to solve the initial value problem. The evaluation of the given numerical solution procedure, by application to benchmark problems, follows in the next chapter.

Chapter 4

Results and Evaluation

4.1 Introduction

The developed FSI algorithm, along with the three upwind schemes, is evaluated via application to problems found in the literature. The predicted results were compared to analytical solutions or experimental data, as well as to the work of other respected researchers. The meshes used for the benchmark problems ranged from structured to unstructured, and solutions were only considered converged once the residual had been reduced by three orders of magnitude, unless otherwise stated. The developed FSI algorithm was found to be robust and accurate with no tuning of parameters required. The analyses were run on a cluster, using 2.1 GHz AMD Opteron Processors operating with shared memory. The evaluation of parallel computing performance falls outside the scope of this project.

4.2 Riemann Shock Tube problem

The Riemann Shock tube problem [60] is a one-dimensional transient case that is useful as an initial test case, as it evaluates a variety of different aspects specific to shock waves in compressible flow, while an analytical solution exists. The premise of the problem is that there is an infinitely long tube with a membrane positioned in the middle as shown in Figure 4.1. The left and right states are set to specific initial conditions, as stipulated in Table 4.1. At $t = 0$, the membrane breaks and shock waves propagate through the domain.

Of the two initial conditions applied in this study, the first case is the simplest and evaluates the ability of each upwind scheme to sharply represent the shock waves. The second case assesses the presence of entropy violations, which will be evident as jump-discontinuities in the sonic rarefaction wave.

For these cases, a structured mesh was used with a mesh size of $N = 101$ nodes (which is similar to others [34]) and a $CFL = 0.85$. The spacial do-

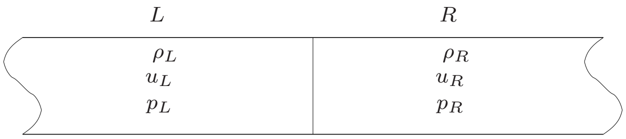

Figure 4.1: Schematic diagram depicting the Riemann Shock Tube problem

Case	ρ_L	u_L	p_L	ρ_R	u_R	p_R
1	1.0	0.0	1.0	0.125	0.0	0.1
2	1.0	0.75	1.0	0.125	0.0	0.1

Table 4.1: Initial values for case 1 and 2 of the Riemann shock tube problem

main is $-0.5 \leq x \leq 0.5$ and the position of the membrane at $t = 0$ is at $x = 0$. The predicted results are shown in Figures 4.2 and 4.3. As depicted, all the implemented upwind schemes exhibited the ability to capture shocks with similar accuracy than that of others [34]. From Figure 4.3 it may be inferred that none of the upwind schemes violated the entropy condition. Lastly, it is evident from Figures 4.2 and 4.3 that each upwind scheme accurately represent the shocks in the domain, as compared to the analytical solution. The Roe and HLLC schemes predicted very similar results, while the AUSM$^+$-up scheme predicted a slightly more accurate result. The relative accuracy and efficiency of the three schemes is rigorously assessed in the following test case via a grid convergence study.

4.3 Forced Oscillation of a NACA0012 Airfoil

Prior to applying the developed ALE flow modelling technology to FSI problems, its ability to predict time-dependent loads on an airfoil undergoing transient accelerations had to be verified. The problem selected was the transonic AGARD test case No. 5 [79], which involved a NACA0012 airfoil undergoing forced sinusoidal pitching in flow at a Mach number of $M_\infty = 0.755$. The angle-of-attack of the airfoil was varied as a function of non-dimensional time t as

$$\alpha = \alpha_0 + \alpha_{max} sin(2k_c t) \tag{4.1}$$

where $k_c = 0.0814$ denotes the reduced frequency, and the mean and maximum angles of attack are $\alpha_0 = 0.016°$ and $\alpha_{max} = 2.51°$, respectively.

The efficacy of the three upwind schemes was evaluated via a grid convergence study as proposed by Raoche [81]. This served to evaluate both relative accuracy of the schemes, as well as to assess the formal order of accuracy and level of certainty of predicted results. For this purpose, a series of unstructured meshes were employed containing 5,000, 10,000, 15,000,

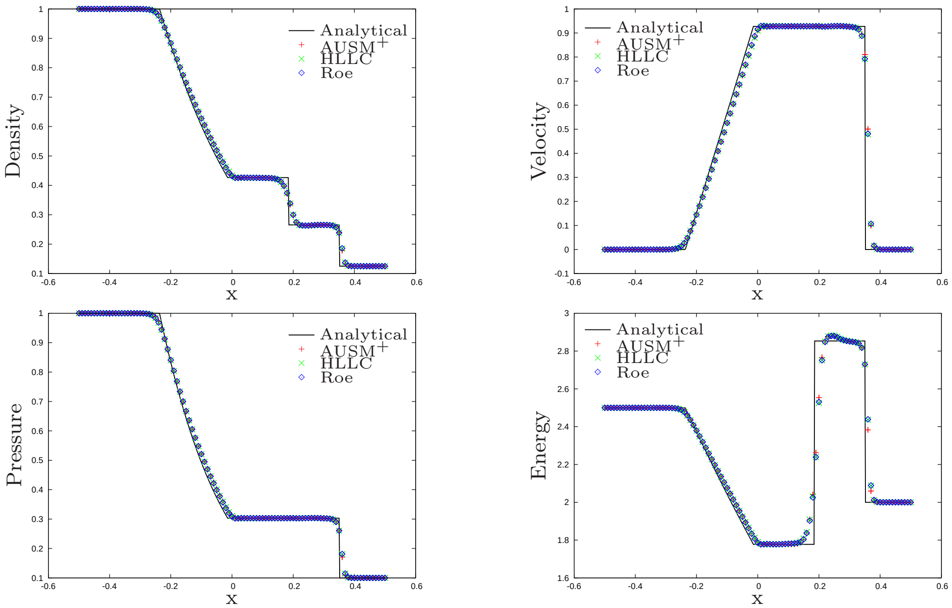

Figure 4.2: Results of the Riemann Shock Tube case 1 at $t = 0.2$

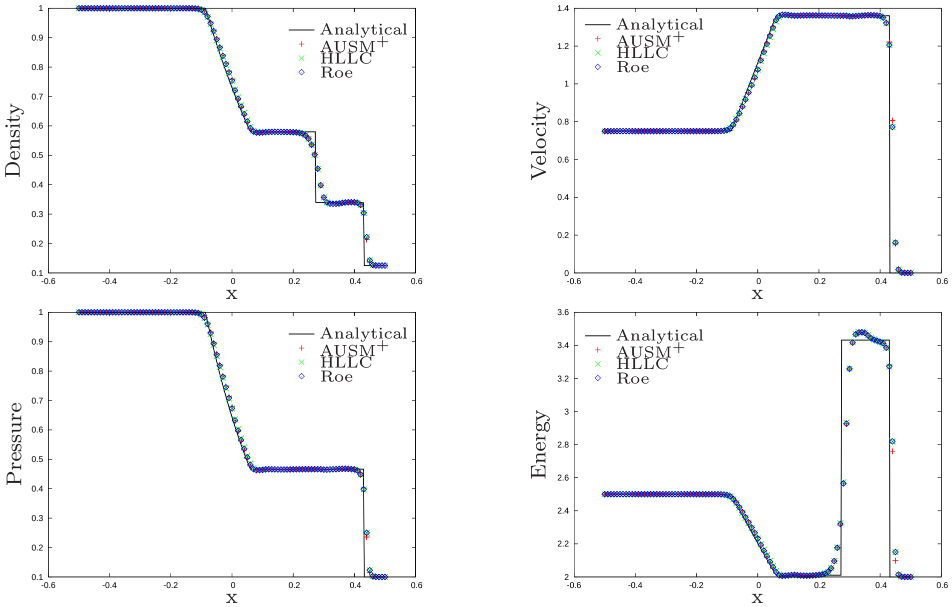

Figure 4.3: Results of the Riemann Shock Tube case 2 at $t = 0.2$

20,000 and 40,000 vertexes, respectively (Fig. 4.4). In the interest of temporal accuracy, the non-dimensional timestep size was $\Delta t = 0.19$, which correlates to 0.5% of a single oscillation. The analyses were run using 46

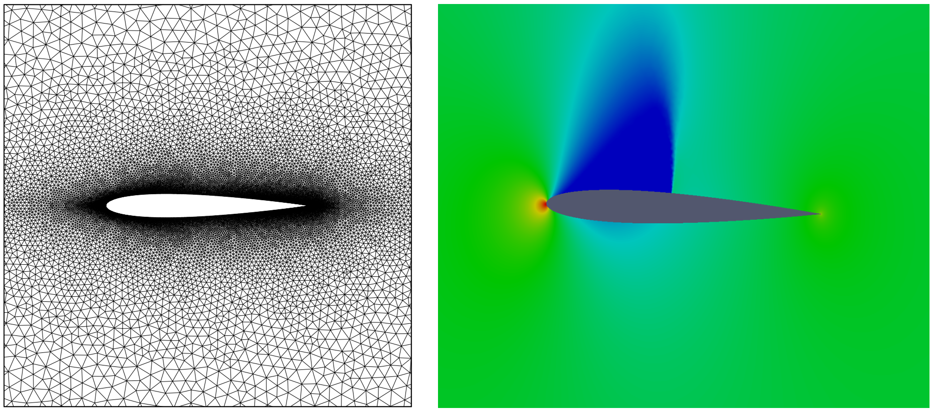

Figure 4.4: (left) Forced Oscillation NACA0012 test-case unstructured mesh consisting of 40,000 vertexes. (right) Pressure contours around the NACA0012 airfoil at $\alpha = 2.51°$

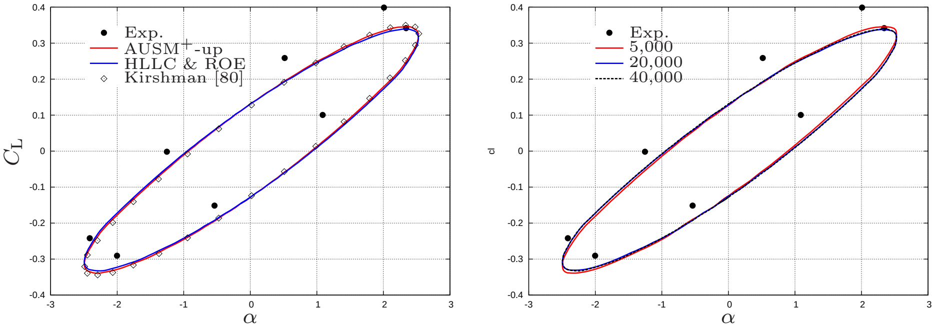

Figure 4.5: (left) Graph of C_{L} versus α for the forced oscillation of the NACA0012 airfoil on a 40,000 node unstructured mesh. (right) Graph comparing the HLLC predicted C_{L} limit-cycle for the 5,000, 20,000 and 40,000 vertex meshes

cores and $CFL = 0.9$.

The pressure contours calculated on the 40,000 mesh were depicted in Figure 4.4. As shown, the sharpness of the shock was accurately captured in the vicinity of the airfoil surface. As expected, smearing was observed as the mesh resolution decreases. With reference to future work, the shock resolution could be maintained with intelligent local mesh refinement.

The predicted lift and moment coefficient limit-cycles are compared to that of others in Figures 4.5 and 4.6. The results were clearly accurate, and revealed that there was a slight difference in the solutions of the AUSM$^+$-up scheme and that of the Roe and HLLC schemes. The disparity was however to within engineering precision (less than 4%). Also noteworthy, particularly

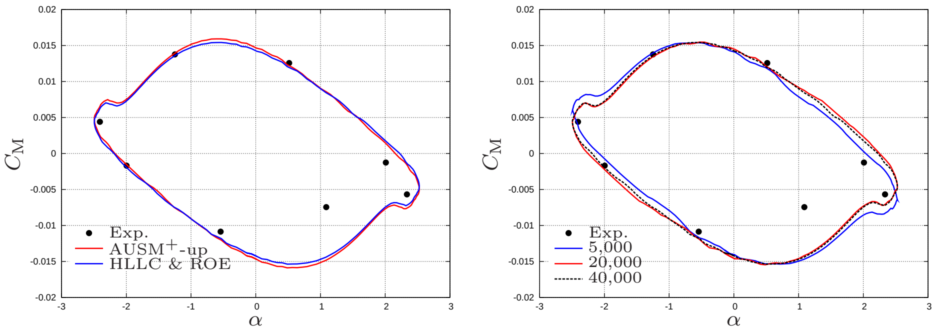

Figure 4.6: (left) Graph of C_{M} versus α for the forced oscillation of the NACA0012 airfoil on a 40,000 node unstructured mesh. (right) Graph comparing the HLLC predicted C_{M} limit-cycle for the 5,000, 20,000 and 40,000 vertex meshes

for the predicted moment evolution, is a seemingly non-physical mild oscillation visible at smaller angles of attack. To highlight the mesh resolution cause of this problem, the moment coefficient limit-cycles predicted using HLLC for the 5,000, 20,000 and 40,000 meshes were compared in Figure 4.6. This demonstrates that the coarser meshes suffer from larger superimposed oscillations with lower frequency. Considering this in conjunction with the oscillations being most pronounced at highest shock translation speed (in the vicinity of zero angle of attack), it is proposed that it is indeed non-physical and likely due to inaccuracies related to shock capturing. In other words, as the shock moves across the mesh, it ”jumps” from one element to another, resulting in artificial effects. For the purpose of future work, it is proposed that this be alleviated via adaptive mesh refinement on the shock.

The total CPU time costs to model seven oscillation cycles are given per mesh and upwind scheme in Table 4.2. The exponential time increase, with the number of vertexes was as expected due to the poor convergence of the simple jacobi solver, which may be addressed in future by employing an advanced solver [82]. Of importance to this work however, was the considerably higher cost (circa 300%) due the AUSM$^+$-up scheme on the coarsest mesh. On investigation, this was found to be the result of the scheme requiring far more iterations per timestep to converge. From this it was concluded that the Roe and HLLC schemes are less sensitive to mesh resolution and thus more robust.

The level of certainty of prediction was quantified via a so-called grid-convergence-index (GCI) which may be calculated from the following equation [81]:

$$\mathrm{GCI} = \mathcal{F}_s \frac{\left|\frac{f_2 - f_1}{f_1}\right|}{\mathtt{r}^{\mathtt{p}} - 1} \tag{4.2}$$

Upwind Scheme	Mesh size (nodes)	Total CPU Hours
Roe	5,000	74.02
	10,000	212.61
	15,000	403.28
	20,000	710.70
	40,000	1969.54
HLLC	5,000	72.46
	10,000	223.87
	15,000	518.38
	20,000	689.99
	40,000	1872.43
AUSM$^+$-up	5,000	199.09
	10,000	280.76
	15,000	309.23
	20,000	673.36
	40,000	1763.41

Table 4.2: Summary of the analysis computational cost for the three upwind schemes

where $\mathcal{F}_s$ is a safety factor and is set to 1.25 for this study. Further, $\mathtt{r}$ and $\mathtt{p}$ are the grid refinement ratio and order of solution (defined below), while f_1 and f_2, respectively, denote the discrete solutions on the fine and coarse meshes. For the GCI calculation, the minimum and maximum lift coefficient, C_{L}, was employed. Note that the minimum and maximum C_{M} only varied from the 3rd significant digit (see Appendix A).

For the purpose of calculating $\mathtt{r}$, the following expression was employed:

$$\mathtt{r} = \left(\frac{N_1}{N_2}\right)^{1/\mathcal{D}} \tag{4.3}$$

where N is the total number of nodes in the mesh and $\mathcal{D}$ is the number of dimensions represented by the mesh. As before, N_1 refers to the finer mesh and N_2 to the coarse mesh. The order of the solution was calculated as

$$\mathtt{p}^{i+1} = \omega \mathtt{p}^i + (1-\omega)\frac{\ln(\theta)}{\ln(\mathtt{r})} \tag{4.4}$$

where $\omega = 0.5$ [81] denotes the relaxation factor and i is the iteration number. Further, $\mathtt{p}^0 = 2$, as the order accuracy was expected to be around second-order. θ was defined as

$$\theta = \frac{(\mathtt{r}_{12}^{\mathtt{p}^i} - 1)}{(\mathtt{r}_{23}^{\mathtt{p}^i} - 1)}\frac{\varepsilon_{23}}{\varepsilon_{12}} \tag{4.5}$$

where

$$\varepsilon_{12} = f_2 - f_1 \qquad \varepsilon_{23} = f_3 - f_2 \tag{4.6}$$

Upwind Scheme	**GCI of Maximum C_L**	**GCI of Minimum C_L**
Roe	0.31%	0.46%
HLLC	0.16%	0.21%
AUSM$^+$-up	0.20%	0.51%

Table 4.3: Summary of the Grid Convergence Study

As stated above, the GCIs for the lift coefficient limit-cycle were calculated using the maximum and minimum lift coefficients. However, as shown in Appendix A, the shock capturing related non-physical oscillations (noted above) resulted in mild nonmonotonic behaviour. As a result, the three most monotone data points were selected for the GCI calculation viz. solutions from the 5,000, 15,000 and 40,000 vertex meshes for HLLC and Roe, and solutions from the 5,000, 10,000 and 20,000 vertex meshes for AUSM$^+$-up.

The resulting GCIs are listed in Table 4.3 and show that a high degree of mesh independence was reached. Further, the HLLC method appears to be superior overall in accuracy and consistency. The oscillations in the moment coefficient limit-cycle made it difficult to evaluate the GCIs. It was however noted, that the maximum and minimum moment coefficient values for HLLC and Roe schemes on the 5,000 and 40,000 vertex meshes were, respectively, within 0.24%. Thus, indicated the solutions for the HLLC and Roe scheme had sufficiently converged. The solutions of the AUSM$^+$-up scheme, on the other hand, varied more yet only within the third decimal place. It therefore again appears, that the AUSM$^+$-up scheme was more sensitive to mesh resolution.

From the above results, it was possible to estimate the order of accuracy of each of the upwind schemes. This was done via approximating the solution at zero grid spacing, f_{extrap}, using Richardson Extrapolation [83] given as

$$f_{extrap} \cong f_1 + \frac{(f_1 - f_2)}{(\mathtt{r}^{\mathtt{p}} - 1)} \tag{4.7}$$

The resulting change in error as a function of, Δx, the average edge length over the surface of the airfoil is plotted in Figure 4.7. As shown, notional second-order accuracy was achieved for all of the evaluated upwind schemes. Though the AUSM$^+$-up scheme appears to have offered superior grid convergence for the maximum lift coefficient, it was also found to be less robust, suffering from excessively slow convergence on coarser meshes as reflected in the CPU times, as well as being the most sensitive to mesh

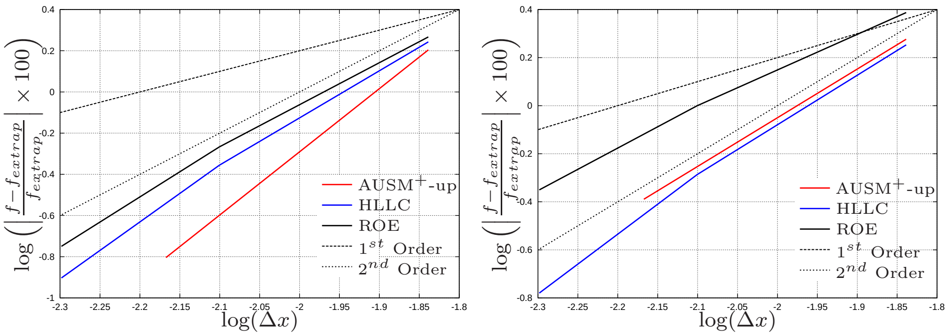

Figure 4.7: Graph of the percentage difference between the discrete f and Richardson Extrapolated f_{extrap} for the (left) maximum and (right) minimum value of C_L

resolution. Overall, HLLC offered competitive accuracy while being robust and achieving engineering precision on the 5,000 node mesh. As a result, this scheme was used in conjunction with the latter mesh for the remainder of the study.

4.4 FSI Spring-Mass NACA64A010 Airfoil

Having validated the flow solver, the last step was evaluation of the FSI capability and of the various structural models. For this purpose, a sub- and transonic test case were considered, and the response predicted via the linear and quadratic ROMs were compared to the analytical version. The mesh employed for these cases was unstructured, consisting of 5,000 vertexes as shown in Figure 4.8. This mesh was selected as it was found to offer engineering precision accuracy in the grid convergence study above. As noted previously, the HLLC scheme was employed due to its balance between accuracy and robustness.

4.4.1 Subsonic Case

The first FSI test case consisted was the subsonic flutter problem for a NACA64A010 airfoil at $M_\infty = 0.3$. The test case was based on the classical incompressible two degrees-of-freedom example of Rodden [84]. For this purpose, damping was included in the structural governing equations with the employed structural parameters being

The reduced frequency, $k_c^2 = 0.196714$, corresponded to the linear flutter speed. The airfoil was given one forced pitching oscillation, employing Equation (4.1), where $\alpha_{\max} = 1.0°$ and the mean angle-of-attack was zero, after which it was allowed to interact freely with the fluid. The flutter response calculated via the linear and quadratic ROMs were compared to the

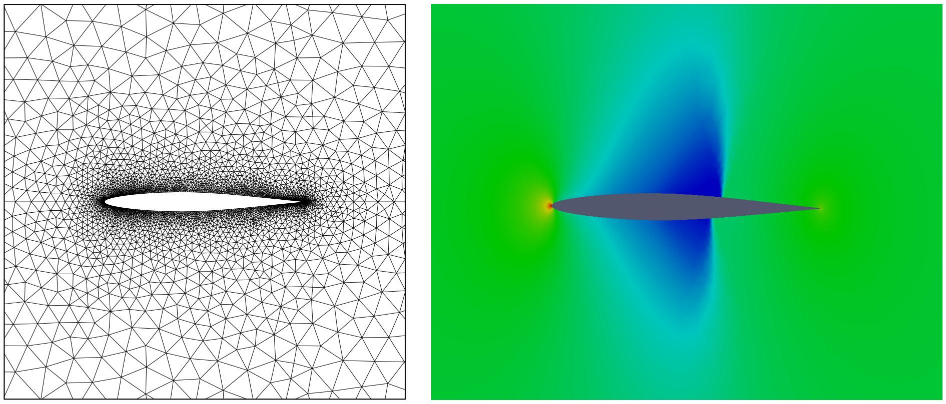

Figure 4.8: (left) Unstructured mesh employed for the sub- and transonic FSI test cases of the NACA64A010 consisting of 5,000 vertexes. (right) Pressure contours around the $M_\infty = 0.82$ case under flutter response at $\alpha = 0.57°$

x_α	r_α^2	$\frac{\omega_h}{\omega_\alpha}$	μ	a
0.1	0.25	0.4	20	0.0

Table 4.4: Structural parameters for the subsonic FSI test case

semi-analytical method in Figures 4.9 and 4.10.

It is noteworthy that the quadratic ROM offered not only an accurate solution for the response of the airfoil, but a significant improvement on the linear ROM. The large rotational component of the airfoil motion in this test case revealed the deficiencies of the linear ROM to describe the deflection of the airfoil for such behaviour. The result was the dramatic artificial damping of the flutter response, which had a significant effect already within the first oscillation, resulting in a large error. Clearly, a linear ROM would be unsuitable as a flutter prediction tool for such cases. The quadratic ROM, on the other hand, conserved the flutter response and proved accurate in predicting the non-linear motion. The developed FSI solver proved to be stable and robust.

4.4.2 Transonic Case

The last FSI test case considered the transonic at $M_\infty = 0.82$ flow over a two-dimensional representation of a swept-wing proposed by Isogai [85]. The structural parameters employed in this test case are given as

As in the former test case, the NACA64A010 airfoil was given one forced oscillation before being released and allowed to naturally respond to the fluid

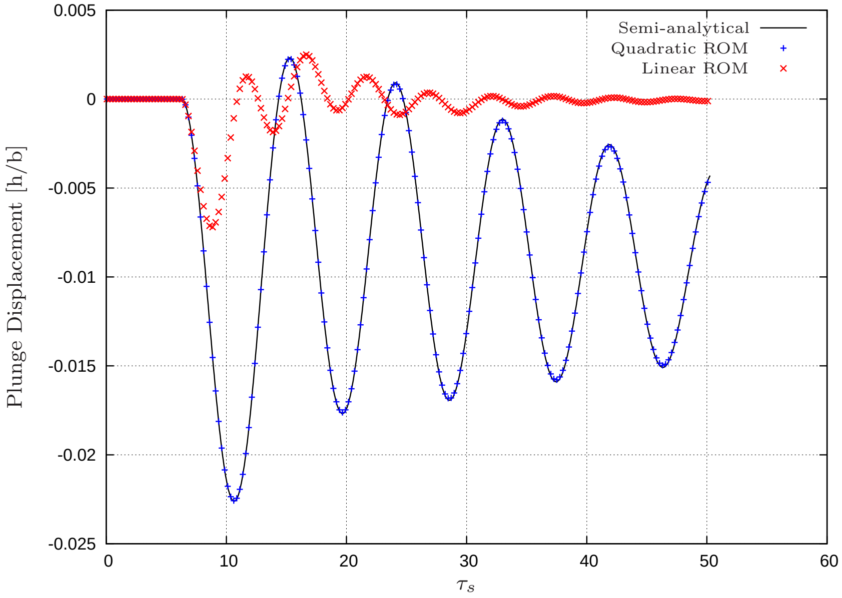

Figure 4.9: Graph of the Plunge Displacement versus time for the NACA64A010 airfoil, $M_\infty = 0.3$

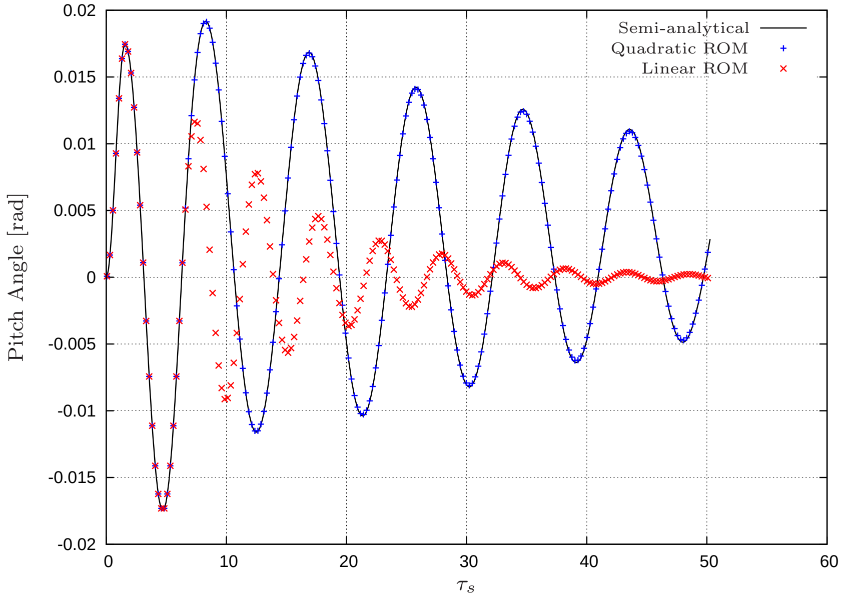

Figure 4.10: Graph of the Pitch Angle versus time for the NACA64A010 airfoil, $M_\infty = 0.3$

x_α	r_α^2	$\frac{\omega_h}{\omega_\alpha}$	μ	a
1.8	3.48	1.0	60	-2.0

Table 4.5: Structural parameters for the transonic swept-wing FSI test case

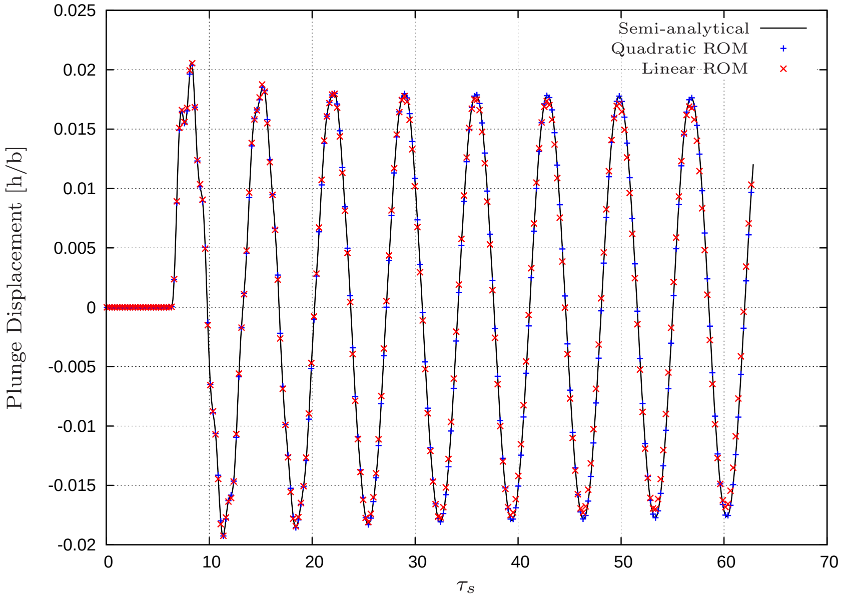

Figure 4.11: Graph of the Plunge Displacement versus time for the NACA64A010 airfoil, $M_\infty = 0.82$

flow. The flutter velocity, V_f, was set to 0.71 in order to obtain a stable response, where the response neither diverges nor decays.

The pressure contours around the airfoil are shown in Figure 4.8, with the sonic shock at the top and bottom surface of the airfoil. Again, the sharpness of the shock decreased further from the surface of the airfoil, this can likewise be improved with intelligent local mesh refinement. The calculated aeroelastic response is shown in Figures 4.11 and 4.12. These results compared well with those of [35] in frequency and amplitude. As before, the quadratic ROM offered an accurate solution and an improvement over the linear ROM by conserving the flutter response. The latter suffered from artificial damping, visibly reducing the amplitude of the response over time. As compared to the subsonic case, the magnitude of the artificial damping was, however, less due to the plunge-dominated deflection of the airfoil. The developed modelling technology was again stable and robust.

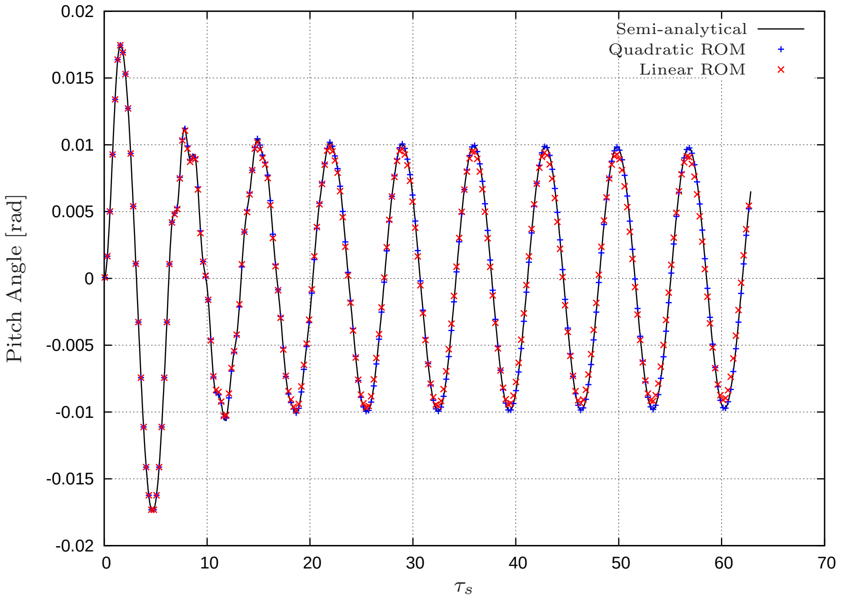

Figure 4.12: Graph of the Pitch Angle versus time for the NACA64A010 airfoil, $M_\infty = 0.82$

4.5 Conclusion

The developed FSI technology presented in this study was validated by application to sub- and transonic non-linear flutter problems. It is demonstrated that the three chosen upwind schemes adequately resolve the shocks in the fluid domain. The grid convergence study identified that the three implemented upwind schemes were notionally second-order accurate and obtained satisfactory solutions for unsteady loading of an airfoil. The HLLC scheme was found to offer the best balance between obtaining asymptotic convergence and robustness. The considered FSI cases proved the developed scheme accurate, robust and stable. Furthermore, the quadratic modal ROM was found to offer dramatic improvements in accuracy over the more conventional linear modal method when significant rotational displacements were present.

Chapter 5

Summary, Conclusions and Recommendations for Future Work

5.1 Summary

The aim of this study was to develop FSI modelling technology to simulate non-linear aeroelastic systems accurately and robustly. The considered non-linearities included transonic shocks in the fluid domain and geometrically non-linear structural responses. The fluid domain was described via an ALE formulation of the unsteady compressible Euler equation set. The latter was discretised via an edge-based vertex centred finite volume method. Three upwind schemes were compared for the purpose of computing the convective fluxes, viz. Roe, HLLC and AUSM$^+$-up. A fourth-order Runge-Kutta dual-time-stepping scheme was employed for the purpose of temporal discretisation. The non-linear structural response was modelled using a quadratic modal reduced-order pitch-plunge model.

The validation of this methodology first considered the fluid and then full FSI systems. The former was evaluated by application to the shock tube problem and the transonic forced oscillation of the NACA0012 airfoil. The shock tube test case showed that shocks in the fluid domain were adequately resolved by all three upwind schemes. These were subsequently applied to modelling the transonic pitching NACA0012 airfoil, and a grid convergence study was preformed. This proved the three schemes notionally second-order accurate, with achieved GCIs less than 1%. The HLLC achieved superior overall performance. The method achieving competitive notional second-order accuracy throughout, while being consistently stable and robust.

5.2 Conclusions

In light of the above, the HLLC scheme was chosen for the aeroelastic test cases. This involved the sub- and transonic flutter response of the NACA64A010 airfoil. The aforementioned highlighted the dramatic superiority of the quadratic ROM over that of the linear method where significant rotational deflection was present. The transonic case showed that the developed FSI technology could successfully resolve the non-linear effects of the moving shocks on the top and bottom of the airfoil. The quadratic ROM still showed an accurate prediction of the solid motion while maintaining an improvement on the linear ROM, although the difference was less apparent due to the largely plunge-dominated deflection.

5.3 Recommendations for Future Work

The following are suggestions to extend this work in the future:

- Extend the FSI algorithm to three dimensions. This will entail extending the fluid solver to include the third dimension and implementing a fully three-dimensional quadratic ROM to resolve the solid deflection.
- The time cost involved in obtaining a solution is to be reduced by the implementation of an advance solver such as Algebraic Multigrid (AMG), Generalised Minimum Residual (GMRES) or a combination of the two where the one preconditions the other. This will reduce the number of iterations needed to drive the residual to the convergence tolerance, thus reducing the time required to complete an analysis.
- When dealing with a sonic shock on the fluid domain, it is important that the mesh resolution in the region of the shock is sufficient to capture the discontinuity. An automated adaptive mesh refinement algorithm could effect this in a computationally effective manner. Careful consideration would be needed to weigh up the improved accuracy and computational cost.

Chapter 6

Appendix A

This appendix contains the graphs of the maximum and minimum values for the lift and moment coefficient limit-cycles. These solutions were calculated on meshes consisting of 5,000, 10,000, 15,000, 20,000 and 40,000 vertexes, respectively.

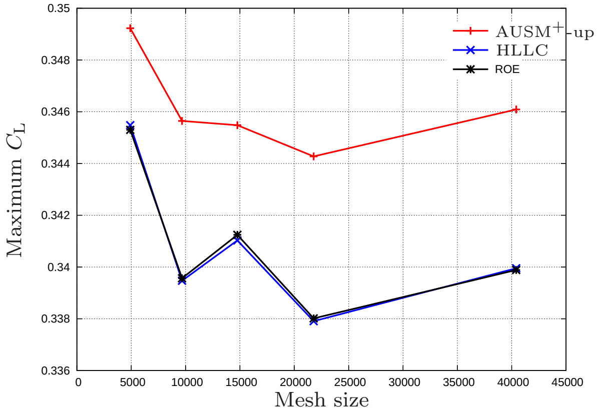

Figure 6.1: Graph of the maximum C_{L} values for the limit-cycles calculated on meshes consisting of 5,000, 10,000, 15,000, 20,000 and 40,000 vertexes, respectively

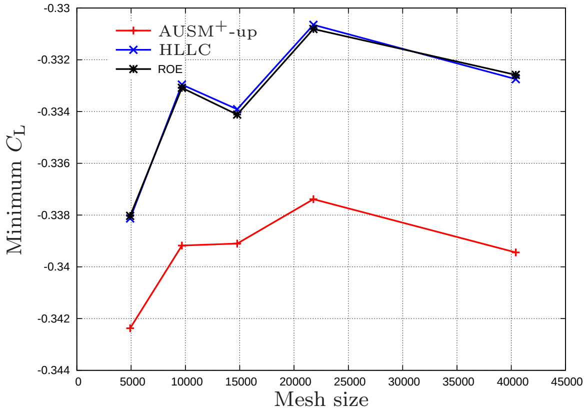

Figure 6.2: Graph of the minimum C_{L} values for the limit-cycles calculated on meshes consisting of 5,000, 10,000, 15,000, 20,000 and 40,000 vertexes, respectively

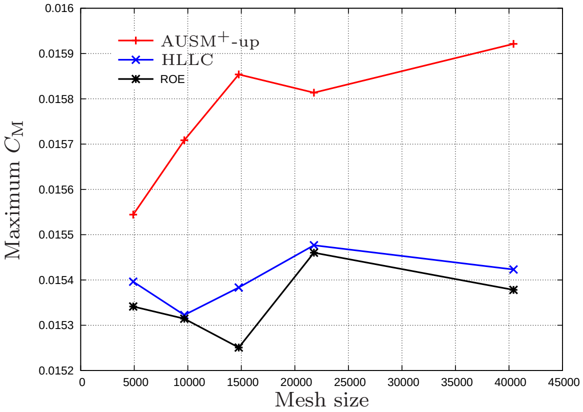

Figure 6.3: Graph of the maximum C_{M} values for the limit-cycles calculated on meshes consisting of 5,000, 10,000, 15,000, 20,000 and 40,000 vertexes, respectively

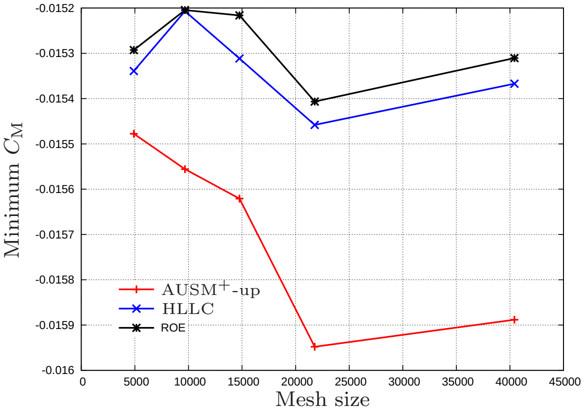

Figure 6.4: Graph of the minimum C_{M} values for the limit-cycles calculated on meshes consisting of 5,000, 10,000, 15,000, 20,000 and 40,000 vertexes, respectively

References

[1] Collar, A. R. (1978). The first 50 years of Aeroelasticity. *Aerospace*, 5(2), 12–20.

[2] Wright, J. and Cooper, J. (2007). *Introduction to Aircraft Aeroelasticity and Loads*. Chichester: John Wiley & Sons Ltd.

[3] Allen, C. B., Taylor, N. V., Fenwick, C. L., et al. (2005). A comparison of full non-linear and reduced order aerodynamic models in control law design using a two-dimensional aerofoil model. *International Journal for Numerical Methods in Engineering*, 64(12), 1628–1648.

[4] Garrick, I. E. and Reed, W. H. (1981). Historical development of aircraft flutter. *Journal of Aircraft*, 18(11), 897–912.

[5] Taylor, N. V., Gaitonde, A. L., Jones, D. P., et al. (2007). Modeling the benchmark active controls wing through linear and computational aeroelastic analyses. *Journal of Aircraft*, 44(4), 1383–1387.

[6] Henshaw, M. J. C., Badcock, K. J., Vio, G. A., et al. (2007). Non-linear aeroelastic prediction for aircraft applications. *Progress in Aerospace Sciences*, 43(4–6), 65–137.

[7] Farhat, C. (2004). *CFD-based Nonlinear Computational Aeroelastics*, vol. 3. Chichester: John Wiley & Sons Ltd.

[8] Guruswamy, G. P. (2002). A review of numerical fluids/structures interface methods for computations using high–fidelity equations. *Computers & Structures*, 80(1), 31–41.

[9] Isogai, K. (1979). On the transonic–dip mechanism of flutter of a sweptback wing. *AIAA Journal*, 17(7), 793–795.

[10] Yurkovich, R. (2003). Status of unsteady aerodynamic prediction for flutter of high–performance aircraft. *Journal of Aircraft*, 40(5), 832–842.

[11] Bennet, R. M. and Edwards, J. W. (1998). An overview of recent developments in computational aeroelasticity. In *Proceedings of the 29th AIAA fluid dynamics conference*. Albuquerque, 15–18 June.

[12] Strgnac, T. W. and Mook, D. T. (1990). Numerical model of unsteady subsonic aeroelastic behaviour. *AIAA Journal*, 28(5), 903–909.

[13] Lee-Raush, E. M. and Batina, J. T. (1993). Wing flutter boundary prediction using unsteady Euler aerodynamic method. In *Proceedings of 34th AIAA/ASME/ASCE/AHS/ASC Structures, Structural Dynamics and Material Conference, and AIAA/ASME Adaptive Structures Forum*. La Jolla, 19–22 April.

[14] Farhat, C., Lesionne, M., and Maman, N. (1995). Mixed explicit/implicit time integration of coupled aeroelastic problems: three-field formulation, geometric conservation and distributed solution. *International Journal for Numerical Methods in Fluids*, 21(10), 807–835.

[15] Piperno, S., Farhat, C., and Larrouturou, B. (1995). Partitioned procedures for the transient solution of coupled aeroelastic problems, Part I: Model problem, theory and two-dimensional application. *Computer Methods in Applied Mechanics and Engineering*, 124(1–2), 79–112.

[16] Lesoinne, M. and Farhat, C. (1998). A higher-order subiteration free staggered algorithm for nonlinear transient aeroelastic problems. *AIAA Journal*, 36(9), 1754–1757.

[17] Felippa, C., Park, K. C., and Farhat, C. (2001). Partitioned analysis of coupled mechanical systems. *Computer Methods in Applied Mechanics and Engineering*, 190(24–25), 3247–3270.

[18] Piperno, S. and Farhat, C. (2001). Partitioned procedures for the transient solution of coupled aeroelastic problems, Part II: Energy transfer analysis and three-dimensional applications. *Computer Methods in Applied Mechanics and Engineering*, 190(24–25), 3147–3170.

[19] Farhat, C., Geuzaine, P., and Brown, G. (2003). Application of a three-field nonlinear fluid–structure formulation to the prediction of the aeroelastic parameters of an F-16 fighter. *Computers and Fluids*, 32(1), 3–29.

[20] Kroyer, R. (2003). FSI analysis in supersonic fluid flow. *Computers and Structures*, 81(8–11), 755–764.

[21] Kamakoti, R. (2004). Fluid-structure interaction for aeroelastic applications. *Progress in Aerospace Sciences*, 40(8), 535–558.

[22] Farhat, C., van der Zee, K. G., and Geuzaine, P. (2006). Provably second-order time-accurate loosely-coupled solution algorithms for transient nonlinear computational aeroelasticity. *Computer Methods in Applied Mechanics and Engineering*, 195(17–18), 1973–2001.

[23] Cavagna, L., Quaranta, G., and Mantegazza, P. (2007). Application of Navier-Stokes simulations for aeroelastic stability assessment in transonic regime. *Computers and Structures*, 85(11–14), 818–832.

[24] Farhat, C. and Lesoinne, M. (2000). Two efficient staggered algorithms for the serial and parallel solution of three-dimensional nonlinear transient aeroelastic problems. *Computer Methods in Applied Mechanics and Engineering*, 182(3–4), 499–515.

[25] Hübner, B., Walhorn, E., and Dinkler, D. (2004). A monolithic approach to fluid-structure interaction using space-time finite elements. *Computer Methods in Applied Mechanics and Engineering*, 193(23–26), 2087–2104.

[26] Greenshields, C. J. and Weller, H. G. (2005). A unified formulation for continuum mechanics applied to fluid–structure interaction in flexible tubes. *International Journal for Numerical Methods in Engineering*, 64(12), 1575–1593.

[27] Dettmer, W. and Peric, J. D. (2006). A computational framework for fluid–structure interaction: Finite element formulation and application. *Computer Methods in Applied Mechanics and Engineering.*, 195(41–43), 5754–5779.

[28] Wall, W. A., Genkinger, S., and Ramm, E. (2007). A strong coupling partitioned approach for fluid–structure interaction with free surfaces. *Computers & Fluids*, 36(1), 169–183.

[29] Le Tallec, P. and Mouro, J. (2001). Fluid structure interaction with large structural displacements. *Computer Methods in Applied Mechanics and Engineering*, 190(24–25), 3039–3067.

[30] Matthies, H. G. and Steindorf, J. (2002). Partitioned but strongly coupled iteration schemes for nonlinear fluid–structure interaction. *Computers and Structures*, 80(27–30), 1991–1999.

[31] Matthies, H. G. and Steindorf, J. (2003). Partitioned strong coupling algorithms for fluid–structure interaction. *Computers and Structures*, 81(8–11), 805–812.

[32] Alonso, J. J. and Jameson, A. (1994). Fully implicit time-marching aeroelastic solutions. In *Proceedings of the 32nd AIAA Aerospace Sciences Meeting and Exhibit*. Reno, 10–13 January.

[33] Willcox, K. and Peraire, J. (1997). Aeroelastic computations in the time domain using unstructured meshes. *International Journal for Numerical Methods in Engineering*, 40(13), 2413–2431.

[34] Luo, H., Baum, J. D., and Löhner, R. (2004). On the computation of multi–material flows using ALE formulation. *Journal of Computational Physics*, 194(1), 304–328.

[35] Mani, K. and Mavriplis, D. J. (2008). Linearization of the coupled unsteady fluid–structure equations: application to flutter control. In *Proceedings of the 26th AIAA Applied Aerodynamics Conference*. Honolulu, 18–21 August.

[36] Schieffer, G., Ray, S., Bramkamp, F. D., et al. (2010). *An Adaptive Implicit Finite Volume Scheme for Compressible Turbulent Flows about Elastic Configurations*, vol. 109. Springer Berlin / Heidelberg.

[37] Blazek, J. (2001). *Computational Fluid Dynamics: Principles and Applications*. Oxford: Elsevier Science, 1st ed.

[38] Malan, A. G. (2002). *Investigation into the Continuum Thermodynamic Modelling of Investment Casting Shell–Mould Drying*. Ph.D. thesis, University of Wales Swansea.

[39] Jameson, A., Schmidt, W., and Turkel, E. (1981). Numerical solutions of the Euler equations by finite volume methods using Runge-Kutta time stepping schemes. In *Proceedings of the 14th AIAA Fluid and Plasma Dynamics Conference*. Palo Alto, 23–25 June.

[40] Liou, M. S. and Steffen, C. J. J. (1993). A new flux splitting scheme. *Journal of Computational Physics*, 107(1), 23–39.

[41] Liou, M. S. (1996). A sequel to AUSM: AUSM+. *Journal of Computational Physics*, 129(2), 364–382.

[42] Liou, M. S. (2006). A sequel to AUSM, part II: AUSM$^+$ -up for all speeds. *Journal of Computational Physics*, 214(1), 137–170.

[43] Jameson, A. (1995). Positive scheme and shock modelling for compressible flows. *International Journal of Numerical Methods in Fluids*, 20(8–9), 743–776.

[44] Godunov, S. K. (1959). A finite-difference method for the numerical computational and discontinuous solutions of the equations of fluid dynamics. *Matematicheskii Sbornik*, 47(89), 271–306.

[45] Roe, P. L. (1981). Approximate riemann solvers, parameter vectors, and difference schemes. *Journal of Computational Physics*, 43(2), 357–372.

[46] Osher, S. and Solomon, F. (1982). Upwind difference schemes for hyperbolic systems of conservation laws. *Mathematics of Computation*, 38(158), 339–374.

[47] Harten, A., Lax, P. D., and Leer, B. V. (1983). On upstream differencing and godunov-type schemes for hyperbolic conservation laws. *Society for Industrial and Applied Mathematics*, 25(1), 35–61.

[48] Toro, E. F., Spruce, M., and Speares, W. (1994). Restoration of the contact surface in the HLL-Riemann solver. *Shock Waves*, 4(1), 25–34.

[49] Harten, A., Engquist, B., Osher, S., et al. (1987). Uniformly high order accurate essentially non-oscillatory schemes III. *Journal of Computational Physics*, 71(2), 231–303.

[50] Swanson, R. C. and Turkel, E. (1992). On central-difference and upwind schemes. *Journal of Computational Physics*, 101(2), 292–306.

[51] Amsallem, D. and Farhat, C. (2008). An interpolation method for adapting reduced-order models and application to aeroelasticity. *AIAA*, 46(7), 1803–1813.

[52] Amsallem, D., Cortial, J., Carlberg, K., et al. (2009). A method for interpolating on manifolds structural dynamics reduced-order models. *International Journal for Numerical Methods in Engineering*, 80(9), 1241–1258.

[53] Ibrahim, R. A. and Woodall, T. D. (1986). Linear and nonlinear modal analysis of aeroelastic structural systems. *Computers & Structures*, 22(4), 699–707.

[54] van Zyl, L. H., Sutherland, A. N., and Rossouw, P. S. (2009). Parabolic mode shapes: what they are, where to get them and what to do with them. In *Proceedings of the International Forum of Aeroelasticity and Structural Dynamic*. Seattle, 21–25 June.

[55] Segalman, D. J. and Dohrmann, C. R. (1996). A method for calculating the dynamics of rotating flexible structures, Part I: Derivation. *Journal of Vibration and Acoustics*, 118(3), 313–317.

[56] Segalman, D. J., Dohrmann, C. R., and Slavin, A. M. (1996). A method for calculating the dynamics of rotating flexible structures, Part II: Example calculations. *Journal of Vibration and Acoustics*, 118(3), 318–322.

[57] van Leer, B. (1979). Toward the ultimate conservative scheme V: A second order sequel to Godunov's method. *Journal of Computational Physics*, 32(1), 101–136.

[58] van Albada, G. D., van Leer, B., and Roberts, W. W. (1982). A comparative study of computational methods in cosmic gas dynamics. *Astronomy and Astrophysics*, 108(1), 76–84.

[59] Dohrmann, C. R. and Segalman, D. J. (1996). *Use of Quadratic Components for Buckling Calculations*. Technical Report No. SAND-96-2367C. Albuquerque: Sandia National Laboratories.

[60] Sod, G. A. (1978). A survey of several of nonlinear finite difference methods hyperbolic conservation for systems laws. *Journal of Computational Physics*, 27(1), 1–31.

[61] Salas, M. D., Jameson, A., and Melnik, R. E. (1983). A comparative study of the nonuniqueness problem of the potential equation. In *Proceedings of the 6th AIAA Computational Fluid Dynamics Conference*. Danvers, 13–15 July.

[62] Clarke, D., Hassan, H., and Salas, M. (1986). Euler calculations for multielement airfoils using Cartesian grids. *AIAA Journal*, 24(3), 353–358.

[63] Sørensen, K. A., Hassan, O., Morgan, K., et al. (2002). Agglomerated multigrid on hybrid unstructured meshes for compressible flow. *International Journal for Numerical Methods in Fluids*, 40(3–4), 593–603.

[64] Malan, A. G., Lewis, R. W., and Nithiarasu, P. (2002). An improved unsteady, unstructured, artificial compressibility, finite volume scheme for viscous incompressible flows: Part I. Theory and implementation. *International Journal for Numerical Methods in Engineering*, 54(5), 695–714.

[65] Lewis, R. W. and Malan, A. G. (2005). Continuum thermodynamic modeling of drying capillary particulate materials via an edge-based algorithm. *Computer Methods in Applied Mechanics and Engineering*, 194(18–20), 2043–2057.

[66] Zhao, Y. and Forhad, A. (2003). A general method for simulation of fluid flows with moving and compliant boundaries on unstructured grids. *Computer Methods in Applied Mechanics and Engineering*, 192(39–40), 4439–4466.

[67] Roe, P. L. and Pike, J. (1985). Efficient construction and utilisation of approximate riemann solutions. In *Proceedings of the Sixth International Symposium on Computing methods in applied sciences and engineering, VI*. Amsterdam, 12–16 December.

[68] Toro, E. F. (1999). *Riemann Solvers and Numerical Methods for Fluid Dynamics – A Practical Introduction*. Berlin: Springer - Verlag, 2nd ed.

[69] Trépanier, J., Reggio, M., Zhang, H., et al. (1991). A finite-volume method for the euler equations on arbitrary lagrangian-eulerian grids. *Computers & Fluids*, 20(4), 399–409.

[70] Harten, A. and Hyman, J. M. (1983). Self adjusting grid methods for one-dimensional hyperbolic conservation laws. *Journal of Computational Physics*, 50(2), 235–269.

[71] Batten, P., Leschziner, M. A., and Goldberg, U. C. (1997). Average-state jacobians and implicit methods for compressible viscous and turbulent flows. *Journal of Computational Physics*, 137(1), 38–78.

[72] Lallemand, M. H., Steve, H., and Dervieux, A. (1992). Unstructured mulitgridding by volume agglomeration: Current status. *Computers and Fluids*, 21(3), 397–433.

[73] Lesoinne, M. and Farhat, C. (1996). Geometric conservation laws for flow problem with moving boundaries and deformable meshes, and their impact on aeroelastic computations. *Computer Methods in Applied Mechanics and Engineering*, 134(1–2), 71–90.

[74] Braess, H. and Wriggers, P. (2000). Arbitrary Lagrangian Eulerian finite element analysis of free surface flow. *Computer Methods in Applied Mechanics and Engineering*, 190(1–2), 95–109.

[75] Farhat, C., Degend, C., Koobus, B., et al. (1998). Torsional springs for two dimensional dynamic unstructured fluid meshes. *Computer Methods in Applied Mechanics and Engineering*, 163(1–4), 231–245.

[76] Oxtoby, O. F. and Malan, A. G. (2010). A fully-coupled, partitioned, finite volume fluid-structure-interaction modelling methodology. *Submitted to International Journal for Numerical Method in Fluids*.

[77] Karypis, G. and Kumar, V. (1999). A fast and high quality multilevel scheme for partitioning irregular graphs. *SIAM Journal on Scientific Computing*, 20(1), 359–392.

[78] Oxtoby, O. F., Malan, A. G., and Nithiarasu, P. (2011). A fully-coupled, partitioned, finite volume fluid–structure-interaction modelling methodology. *Submitted to International Journal for Numerical Methods In Engineering*.

[79] Panel, A. F. D. (1982). *Compendium of Unsteady Aerodynamic Measurements*. AGARD Report No. 702.

[80] Kirshman, D. J. and Liu, F. (2004). Flutter prediction by a Cartesian mesh Euler method with small perturbation gridless boundary conditions. In *Proceedings of the 42nd AIAA Aerospace Sciences Meeting and Exhibit*. Reno, 5–8 January.

[81] Roache, P. J. (1997). Quantification of uncertainty in computational fluid dynamics. *Annual Review of Fluid Mechanics*, 29(1), 123–160.

[82] Pattinson, J., Malan, A. G., and Meyer, J. P. (2007). A cut-cell non-conforming cartesian mesh method for compressible and incompressible flow. *International Journal for Numerical Methods in Engineering*, 72(11), 1332–1354.

[83] Richardson, L. F. (1927). The deferred approach to the limit. Part I. single lattice. Part II. interpenetrating lattices. *Philosophical Transactions of the Royal Society of London*, 226(1), 299–361.

[84] Rodden, W. P. and Bellinger, E. D. (1982). Aerodynamic lag functions, divergence, and the British flutter method. *Journal of Aircraft*, 19(7), 596–598.

[85] Isogai, K. (1981). Transonic dip mechanism of flutter of a sweptback wing: Part II. *AIAA Journal*, 19(9), 1240–1242.